Soft Matter

PAPER

View Article Online
View Journal | View Issue

Cite this: *Soft Matter*, 2026, **22**, 3692

Overview: the Janus-nature of molecular CO_2 in charge adjustment at wet surfaces

Peter Vogel, †[a] Muhammad Nawaz Qaisrani,†[b] Mattis Rasenat,[a] Johannes Lützenkirchen, [c] Marialore Sulpizi,[d] David Beyer, [e] Christian Holm [e] and Thomas Palberg *[a]

Received 14th March 2026,
Accepted 5th May 2026

DOI: 10.1039/d6sm00222f

rsc.li/soft-matter-journal

Molecular CO_2 readily dissolves in aqueous electrolyte solutions and partially dissociating to form carbonic acid. The decharging effects of the dissociation products mediated by the ensuing pH-shift and the additional salinity are well established. However, the effects of dissolved molecular CO_2 have not been studied systematically. We summarize recent and novel investigations on the role of CO_2 regarding charge control at surfaces submersed in aqueous electrolytes. In our electrokinetic and conductometric measurements on representative surfaces, we took special care to control and monitor the electrolyte composition *in situ*. We discriminate the effects of molecular and dissociated CO_2 *via* control experiments using HCl. Depending on the surface under investigation and the charging mechanisms involved, we find that molecular CO_2 assists either charging, de-charging and/or recharging. This contrasting charge regulating behaviour reveals the Janus nature of dissolved molecular CO_2 with respect to charge control at wet surfaces. In our complementary molecular dynamics simulations, Q4 silica and 9% ionized Q3 silica surfaces are studied as hydrophobic/hydrophilic, respectively charged/uncharged, analogues, as well as uncharged Q3 silica and molecularly rough Isoleucin-coated quartz surfaces. In all cases, we find that the charge-neutral CO_2 molecule physisorbs in a thin diffusive layer close to the surface, which leads to pronounced re-structuring of the electric double layer. Based on this result, we suggest to interpret the experimentally observed Janus nature of molecular CO_2 in terms of a local decrease of the dielectric permittivity. This in turn leads to a local strengthening of electrostatic interactions dominating the double layer structure next to charged surfaces. Specifically, we propose that CO_2 induces a dielectric charge regulation for weakly acidic surface groups, assists the incorporation of OH^- into the H-bond network at smooth inert surfaces, and induces significant ion-correlations promoting co-ion binding. Overall, we demonstrate that molecular CO_2 allows for a controlled charge-adjustment in opposing directions. We anticipate that our findings on the one hand provide substantial challenges for analytical or numerical modelling as well as for controlled experimental work, but on the other hand bear important practical implications for applications ranging from desalination to bio-membranes.

Introduction

Functional dielectric surfaces in contact with aqueous electrolytes are ubiquitous, with examples ranging from our lungs over desalination facilities to colloidal suspensions and emulsions. Many of these surfaces owe their specific function to the presence of charges. The ways to acquire these are manifold. Well known examples include the dissociation of ionogenic surface groups or the desorption/adsorption of lattice ions,[1] but also further "chemical or physical" mechanisms[2] have been studied, like the adsorption of co-ions,[3–6] multivalent counterions[7] or surfactants[8] from solution, photochemistry,[9] piezoelectricity or slide electrification.[10] A particularly interesting mechanism is the adsorption of protons or hydroxyl ions stemming from water hydrolysis, which is suspected to give rise to surface charges at chemically inert surfaces even in the absence of other salts.[11] This has been studied both spectroscopically[12] and by electrokinetic experiments.[13] Computer simulations further suggest that at specific oxide

---

[a] *Institute of Physics, Johannes Gutenberg University, Mainz, Germany. E-mail: palberg@uni-mainz.de*
[b] *Institute of Physics and Institute of Micro- and Nanotechnologies, Technische Universität, Ilmenau, Germany*
[c] *Institute for Nuclear Waste Disposal (INE), Karlsruhe Institute of Technology (KIT), Karlsruhe, Germany*
[d] *Department of Physics, Ruhr Universität Bochum, Bochum, Germany*
[e] *Institute of Computational Physics (ICP), University Stuttgart, Stuttgart, Germany*

† Both authors contributed equally.

surfaces, an integration of hydroxyl ions into the hydrogen bond network of the first water layer might occur even under neutral pH conditions.[14]

In general, the obtained charge state depends on the details of both surface chemistry and electrolyte composition. It can be manipulated by appropriately adjusting surface and environmental conditions, *i.e.*, surface hydrophobicity, dielectric permittivity, softness and roughness as well as salinity,[15] pH,[16,17] or temperature.[18] Next to hydrolysis products, deliberate additives and/or contaminations, the aqueous electrolyte often contains dissolved gases. Distilled water may store gases in larger amounts (molar fraction solubilities for CO_2, O_2, N_2 and Ar at 298.15 K and atmospheric pressure (101.325 kPa) are 61.48×10^{-5}, 9.1×10^{-5}, 1.17×10^{-5}, and 2.5319×10^{-5} respectively[19]), but given the composition of ambient air, CO_2, O_2, and N_2 are most prominent. Their ability to adsorb at hydrophobic surfaces is promoted by a depletion of water in the immediate vicinity of such surfaces.[20,21] It is, however still under discussion, whether the adsorbed gases form condensed films, nanobubbles, or stay in solution as diffuse gas-enriched layers close to the surface.[22–26] In their presence soft polymeric surfaces appear to be very smooth, while such surfaces in contact with degassed water reveal a (reversible) nano-scale corrugation.[27,28] This mechanical effect was suggested to be mediated by a thin film of gas forming at hydrophobic surfaces. Dissolved gases, moreover, also influence the stabilization of hydrophobic colloids. Experiments not discriminating gas species showed pronounced increases in the flocculation for paraffin particles[29] as well as oil in water emulsions,[30–32] when these were allowed contact with ambient air.

Gas-species-specific studies typically concentrate on the case of airborne CO_2. Molecular CO_2 readily dissolves in water, where it partially reacts to form carbonic acid, which subsequently dissociates.[33] Under so-called realistic salt-free conditions (*i.e.*, deionized water equilibrated at ambient air), one has a pH of 5.5 and about 3.16 μmol L^{-1} of additional electrolyte.[34] Both parameters are well known to interfere with surface electro-statics. The acidification in particular triggers pH-driven surface charge regulation. Here, the degree of regulation depends on the chemical nature of the surface, and for colloidal systems further on the amount of double layer overlap.[35–37] A special case are calcite surfaces, where CO_2 and its dissociation products can chemically interfere with CO_3^{2-}, which is one of the lattice ions.[38] An altered bare surface charge in turn affects adsorption, interparticle forces, colloidal stability, and deposition phenomena.[39,40] Moreover, *via* screening effects, the additional ionic content decreases the effective charges, Z_ζ and Z_σ, as determined from electrokinetic investigations *via* the ζ-potential[41] and from conductometric experiments in terms of the number of freely mobile counter-ions, respectively.[42,43] An equivalent effect is seen in the so-called renormalized charge, Z_{PBC} obtained from solving the Poisson Boltzmann equation under charge regulation boundary conditions.[34,39,44,45] Finally, in strongly interacting colloidal systems, also the effective interaction charges, which additionally account for many body interactions,[46–48] are substantially decreased. Clearly, the charge regulation and screening effects of the dissociation products of CO_2 are well-established and can be accommodated in theoretical treatments.

In contrast, much less is known about the influence of molecular CO_2, even though it readily adsorbs at various surfaces including the aforementioned hydrophobic surfaces, but also hydrogels and metal electrodes.[24,49] While physisorption of CO_2 has been subject of growing interest due to climate issues,[50] the influence of physisorbed CO_2 on the capturing surface has been left widely unexplored. CO_2 molecules are non-polar, but polarizable due to the presence of oxygen at the extremes. Thus, the presence of polar compounds at solid surfaces may polarize the CO_2 electron-cloud, facilitate induced dipole–dipole interaction and/or the formation of hydrogen bonds and influence the structure of the electrical double layer (EDL) close to the surface.[51,52] However, such effects compete with those of the dissociation products and are observable only at low to vanishing salinity and close to neutral pH values. Still, and despite preparational difficulties, a number of studies points in that direction.

At gold electrodes, CO_2 was shown to modulate the electrochemical capacitance of the EDL, which may bear important practical implications for mitigating greenhouse gas emissions.[25] Further, contrasting charge characterization experiments performed under strictly CO_2-free conditions and after equilibration against ambient air, some quantitative inconsistencies are observed,[53] which cannot be explained by standard electrokinetic theory[42,54] and its extensions using EDL models accounting only for the dissociation products.[34] Specifically, charges from different approaches do not agree and in the absence of CO_2 one observes a non-monotonic particle concentration dependence in the ζ-potential of charged spheres with very low potentials for isolated particles.[55–58] Moreover, the presence of CO_2 appears to influence the adsorption of ions from solution. Particle charging by adsorption of co-ionic surfactants[59] works well when particles are suspended in standard distilled water, but fails under CO_2-free conditions.[60] Negatively charged particles suspended in salt free water in contact with ambient air, show mobility, respectively ζ-potential extrema upon the addition of micro-ions.[3,4,61–64] Mobility maxima may occur for a number of reasons, including EDL relaxation effects at constant charge,[65] hairy layers and other influences of surface conditions.[61,66] Extrema of the ζ-potential cannot be explained assuming constant surface properties and thus indicate ion adsorption. Potential minima and even charge reversal are observed for multivalent counter-ions.[65,67,68] For potential maxima, the favored explanation is the adsorption of co-ions[69–71] even though in some studies the position and shape of the maxima would not show any dependence on co-ion type.[3] Conversely, in studies performed under strictly de-carbonized conditions, no potential maxima have thus far been observed.[72–74]

Relating conditioning procedures employed and results obtained in these investigations points to a significant, if not dominant influence of molecular CO_2 on the various charging processes possible for surfaces in contact with aqueous electrolytes. However, systematic studies comparing different surface types under variable CO_2 content, salt concentration and pH are missing. Consequently, a more comprehensive investigation and understanding of the role of CO_2 for the charge adjustment of surfaces are still highly desired.

In the present paper, on occasion of this special issue dedicated to late Stefan U. Egelhaaf, we take the chance to review our own targeted attempts made over the past years in that direction and to complement these with new experimental findings as well as extended computer simulations. Both will then allow developing a consistent picture of the ways and the effectiveness of charge manipulation by dissolved molecular CO_2.

Some indispensable experimental prerequisites for our studies were realized in close and continuous collaboration and exchange with Stefan and are shortly recalled in the instrumental developments section. The first relates to the reliable adjustment and monitoring of salinity, pH and CO_2-concentration in the water being in contact with the surfaces under investigation. Over time, the basic version of the gas-tight conditioning circuit[75] was extended by integrated *in situ* optical and conductivity measurements,[43,76] and more recently, also by a photometric pH determination.[77] Further routine cross-checks of obtained data by numerical calculations using the freeware program Aqion were introduced.[78] Second, we improved our Doppler velocimetry[79] to cope with multiple scattering systems,[80] thus enlarging the range of accessible particle concentrations. Finally, we devised an optical cell with exchangeable side walls,[81] which for the first time allowed for simultaneous studies of suspension electrophoretic and wall electro-osmotic mobilities. Exploiting this improved experimental instrumentation, we began with systematic investigations. In a first study,[82] we compared the electro-kinetics of surfaces under de-carbonized conditions to surfaces in contact with water equilibrated to ambient air. There we compared hydrophilic SiO_2, a hydrophobic copolymer and a superhydrophobic surface upon addition of NaCl and HCl. While the focus was on CO_2 induced decharging processes, we also found evidence of subsequent re-charging. Molecular dynamics simulations suggested to relate the experimental results to the formation of a diffuse layer of molecular CO_2 forming close to the solid surface. The following study[83] was restricted to SiO_2 and the copolymer surface, but significantly extended the range of accessible CO_2 concentrations. Interestingly, nearly complete decharging could be observed under over-carbonized conditions followed by re-charging upon the successive addition of NaCl or HCl. Comparing the evolution of ζ-potentials upon addition of different electrolytes allowed discrimination of different decharging mechanisms and gave the relative magnitudes of decharging by screening, pH-driven charge regulation and CO_2-induced charge regulation. The third of our previous studies aimed at a comprehensive charge characterization.[84] Effective and bare charges as well as surface group densities were obtained from conductometric experiments in dependence on particle concentration, electrolyte concentration within the series LiCl, NaCl, KCl, CsCl, and amount of added NaOH, respectively. Experiments were accompanied by numerical calculations using a Poisson Boltzmann cell model under charge regulating boundary conditions to infer the effective pK_a shift of surface groups as induced by the presence of CO_2. A consistent description of the drastic decharging of surfaces bearing weakly acidic surface groups by molecular CO_2 as well as the corresponding decrease in the conductivity charge and the disappearance of counter-ion exchange was obtained. We further made a first suggestion for an underlying novel charge regulating mechanism.

We complement these previous findings by presenting new and extended experimental results regarding CO_2-assisted (re-)charging by anion-adsorption and by reporting extensive systematic simulation results providing insights at the molecular level. In the experiments, we again vary the type and amount of added 1 : 1 electrolyte under continuous *in situ* control of pH and conductivity. We consider thoroughly decarbonized samples, samples equilibrated in contact with ambient air and samples with variable CO_2 content. As before, we compare hydrophobic to hydrophilic as well as polymeric to oxidic surface materials. We focus on three materials featuring three representative charging mechanisms: (i) chemically inert sapphire (0001) charges by adsorption of hydroxyl ions from solution. Comparing the ζ-potentials of sapphire in the absence and in the presence of dissolved CO_2 tests its influence on the charging of this chemically inert surface in salt-free water. (ii) carboxylate-stabilized polymer colloids and (iii) fused silica bearing hydroxyl groups both charge by surface group dissociation, de-charge under the influence of CO_2 but, in addition, can be charged by co-ion adsorption. Here, ζ-potentials obtained for silica and polymer surfaces under addition of electrolytes from the lyotropic series NaF, NaCl, NaBr, NaI, at different levels of CO_2 reveal the complex interplay of hydrophobicity, co-ion type and diffusely adsorbed CO_2 for the recharging of surfaces by anion adsorption.

Complementary microscopic information is obtained from molecular dynamics simulations of different hydrophobic/hydrophilic, respectively charged/uncharged surfaces at various salt and CO_2 concentrations. In an earlier paper we had shown the tendency of molecular CO_2 to enrich in a thin layer close to the surface.[82] Our new simulations repeat the elder ones with significantly increased run durations and better statistics and further include added salt alt various concentrations. Specifically, Isoleucin coated quartz surfaces are compared to inert Q4 silica, hydrophilic but charge-neutral Q3 silica and 9% ionized Q3 silica. This choice represents close analogues of the experimentally investigated surfaces. Water is described by the TIP3P model to account for steric, electrostatic and dipolar interactions. Simulations in water with and without CO_2 show the dependence of the amount of diffusively adsorbed CO_2 on surface hydrophobicity and charge. Runs at increasing salt concentrations shed light on the supporting role of salt for CO_2 enrichment. Comparison of runs with and without CO_2 reveals the subtle changes in the EDL structure caused by the presence of CO_2 and allows estimates of the relative amount of condensed and free ions as well as checks for charging by co-ion adsorption.

We here combine our comprehensive experimental data base with the findings made in the simulations. This facilitates the development of a consistent picture of the ways and the effectiveness of charge manipulation by CO_2 for a first set of representative charging and charge-regulating mechanisms. The basic underlying suggestion is a local lowering of the dielectric permittivity by the formation of the CO_2-enrichment layer close to surfaces, which results in a strengthening of interactions directly and indirectly related to electrostatics. Depending on the specific charging mechanism under consideration, this may influence the surface charge in opposite directions and establishes the Janus nature of molecular CO_2 regarding charge adjustment.

Interestingly, this broad and profound impact of molecular CO_2 had received only little attention in previous studies. Presumably due to the difficulties in controlling the level of dissolved CO_2 as well as in discriminating its effects from those of its dissociation products. However, even with the present approach, much work on additional surface types, other types of additives, a wider pH range and higher salinities remains to be done. In the long run, our observations should trigger much interest in a deeper theoretical understanding and its implementation in future modelling. Moreover, they should motivate a careful re-check of previous results obtained under less well controlled CO_2 concentrations We expect that both is of great importance for improving and optimizing the performance of functional surfaces in practical applications.

In the following, we first recall the most important instrumental developments facilitating our systematic investigations. We then show the experimental results from conductometry and electrophoresis and present the outcome of the computer simulations. We note that we group the results thematically, rather than historically and only where appropriate, we give reference to the quoted papers. In the discussion section, we detail and rationalize the effects of molecular CO_2 on the various surfaces and charging mechanisms. Further, we point out several implications for future research and potential application. In our conclusions, we summarize and emphasize the main finding of the present study, namely, that CO_2 plays an important, Janus-type role in charge control for a large variety of surfaces in contact with water.

Materials and experimental developments

Samples and sample conditioning

Spherical copolymer particles were kindly provided by BASF, Ludwigshafen (Lab code PNBAPS359, manufacturer batch number 2168/7390). Particles there had been synthesized by radical emulsion-polymerization from 60% w/w butylacrylamid, 38% w/w styrene, 2% w/w acrylic acid, and 0,5% w/w sodium-peroxodisulfate. The particles are electrostatically stabilized by $N = (134 \pm 2) \times 10^3$ carboxylate surface groups as determined *via* conductometric titration.[84] Their diameter of $2a = 359$ nm was determined by the manufacturer using analytical ultracentrifugation. Stock suspensions of particle number densities $n \approx 10^{18}$ m^{-3} were prepared by dilution with doubly distilled (DI) water. Subsequently, mixed-bed ion exchange resin (IEX) (Amberjet, Carl Roth GmbH + Co. KG, Karlsruhe, Germany) was added and the suspensions were left to stand under occasional stirring for some weeks. They were then coarsely filtered using Sartorius 5 μm syringe-driven membrane filters to remove dust, ion-exchange debris, and coagulate regularly occurring upon first contact with IEX.

All further sample preparation/conditioning steps including the conductivity measurements were performed in a peristaltically driven circuit described in detail elsewhere[75,76] (see also the sketch in Fig. S1 of the SI). Briefly, air-tight Teflon® tubings and valves [Bohländer, Germany] connect (i) a reservoir under inert gas atmosphere (Ar) to add further particles, water, chemicals and/or CO_2 gas, (ii) a mixed-bed ion-exchange resin-filled column (IEX, Amberlite K306, Carl Roth GmbH Co. KG, Karlsruhe, Germany), (iii) a conductivity measurement (see below) and (iv) an arbitrary number of optical cells facilitating further simultaneous experiments at identical conditions. The latter typically include a turbidity or static light scattering experiment to determine the particle concentration, a photometric experiment for pH determination (see below) and an optical cell for electro-kinetic experiments based on Laser Doppler Velocimetry (see below) made of fused silica (EL10 by Rank Bros., Bottisham, Cambridge, UK or replica by Lightpath Optical Ltd., Milton Keynes, UK). The fluid volume of the circuit is on the order of 50–100 mL, depending on the size and amount of measuring cells implemented, the fill height of the reservoir and the amount of IEX added. The volume difference between bypass and IEX column is on the order of 15–25 mL. The exact volumina are determined from weighing.

Fused silica provides the charged hydrophilic model surface, electrostatically stabilized by hydroxyl groups. Its state of dissociation is determined by the pH of the adjacent electrolyte. Corresponding electrokinetic properties have been determined in a large number of studies.[85] While some minor, conditioning-related differences are often observed, in general, the isoelectric point is agreed to be around pH 3.[86] The cells were cleaned by heating in a flame of a gas burner for some 15 min, left to cool and successively sonicated for 60 min at 35 °C in 2% alkaline detergent solution (Hellmanex III, Hellma Analytics). They were further rinsed with DI water and dried in a nitrogen stream.

For measurements on sapphire as inert oxide surface, the Rank cell was replaced by a custom-made cell with exchangeable side walls (see below). Sapphire (0001) single crystals were obtained from MaTeck (Jülich, Germany). The single crystals were 75 mm by 26 mm and 0.5 mm thick, polished on two sides. Before mounting, samples were cleaned according to Rabung *et al.*,[87] to eliminate all organic carbon contamination and minimize inorganic contamination, *i.e.*, samples were soaked in acetone overnight, subsequentl washed and soaked with ethanol for 2 h, and finally washed and soaked with MilliQ water for 1 h.

After circuit assembly and tightness check (water conductivity σ_{H_2O} = 55 nS cm^{-1}), an appropriately diluted stock suspension is loaded into the circuit under filtering with Sartorius 1.2 μm and 0.8 μm filters. Its volume is determined by weighing, with the particle concentration checked by turbidity. The suspension is then thoroughly deionized, while passing through the IEX column. After attaining fully deionized and decarbonized conditions, the desired amounts of salt solutions can be injected through a septum into the reservoir. The sample is then homogenized again by pumping under *in situ* control of conductivity, turbidity and pH, while the IEX column is now bypassed. Alternatively, the Ar can be successively replaced by CO_2–gas. The approach to an almost pure CO_2 atmosphere, however, is restricted by the onset of coagulation of the tracer particles. the minimum pH reached under over-carbonized conditions was pH = 4.8 and the maximum conductivity value amounted to σ = 38 μS cm^{-1}. According to aqion, this corresponds to a partial pressure of $p_{CO_2} \approx 1.8 \times 10^{-2}$ atm and $pCO_2 \approx 1.7$.

Total micro-ion concentration

To allow comparison of different electrolyte types in dependence on a single control-parameter in the results section, we display some of our observations in dependence on the total concentration of micro-ions. This important quantity is calculated respecting the contributions of all detectable micro-ionic species in solution, *i.e.*, the tracer particle counter-ions, the added electrolyte ions, and the H^+ and OH^- ions stemming from water hydrolysis. We note that this neglects wall-counter-ions, since their contribution of is not resolvable in bulk measurements. Similarly, the very small amounts of residual impurities (*e.g.* typically $<10^{-8}$ mol L^{-1} of ions leaking from the container walls[90]) is not considered in calculating the total micro-ion concentration.

The concentrations of the remaining ions are determined using suitable combinations of precisely determined added quantities with conductivity measurements evaluated by Hessinger's model of independent ion migration, classic or photometric pH measurements evaluated using the freeware aqion program, and, where necessary electrophoretic mobility measurements further evaluated for the effective tracer charge (see below). If not all of these measures were needed, the remaining ones were used for cross-checking the results. Therefore, the integration of all these measurements in to our air-tight conditioning circuit is indispensable.

To be specific, the total concentration of H^+ is inferred from the pH readings. From this, the concentration of OH^- is inferred using the water dissociation product. The concentrations of halide (F^-, Cl^-, Br^-, I^-) and alkali (Li^+, Na^+, K^+, Cs^+) ions are taken from the volume and concentration of the added electrolytes.

The total concentration of H^+ originates from different sources and one needs to severally discriminate their contributions. Here we make use of the fact that neutral salts do not contribute to the pH. Moreover, electroneutrality requires equal amounts of cations and anions, including the macro-ions, if present. In the presence of tracers with their weak acid groups, the calculation of the tracer counter-ion contribution to the total H^+ concentration affords additional knowledge of both tracer density and effective charge. While the former can be determined independently (*e.g.* from turbidity) the latter requires an iterative procedure to calculate it from the measured tracer mobility. That calculation involves the Debye screening parameter which in an initial approximation is estimated using twice the total proton concentration. After obtaining a value for the effective tracer charge and thus a value for the concentration of counter-ions balanced by macro-ions, that concentration is subtracted from the initial input and the charge calculation repeated with a new Debye parameter. Convergence is typically obtained after a few steps. Tracer density times tracer effective charge then yields the tracer counter-ion contribution to the total H^+ concentration.

Added HCl is assumed to be fully dissociated under all here investigated conditions. The concentration of H^+ from that source is simply equated to the concentration of Cl^- and subtracted from the tracer counter-ion contribution corrected H^+-concentration. Electroneutrality, then, requires that the remaining H^+ function to balance the anions present from CO_3H^- and $CO_3{}^{2-}$ formed upon the dissolution of molecular CO_2.[33] The small amounts of divalent anions were not discernible in the conductivity measurements, despite their larger valence. Also, aqion calculations show that the carbonate concentration is extremely small already at pH neutral conditions and decreases further as the pH decreases. It was therefore regarded negligible compared to the amounts of H^+ from other sources. The only remaining source of protons is carbonic acid. The bicarbonate concentration then equals the total H^+ concentration corrected for the H^+ concentrations related to the presence of tracers and hydrochloric acid. For orientation, under ambient (over-carbonized) conditions dissociated carbonic acid contributes 6.3 μmol L^{-1} (32,6 μmol L^{-1}) to the total micro-ion concentration.

In addition to being fast, versatile and reproducible, circuit conditioning thus allows for a comprehensive quantitative characterization of the electrolyte concentration and composition. In the present study it facilitates a reliable comparison of surface charges and charging mechanisms in systems containing different but well controlled concentrations of CO_2 and/or added electrolytes.

Conductometry

Bulk conductivities, σ, were measured at a frequency of ω = 400 Hz (electrodes LTA01 and LR325/01 with bridge LF538 or electrode LR325/001 with bridge LF340, WTW, Germany). This frequency is low enough to stay in the DC-limit, but large enough to avoid electrode polarization effects. Since the conductivity increases with increasing temperature,[88] care was taken to maintain a constant temperature of (25 ± 0.5) °C. Data are interpreted in terms of Hessinger's conductivity model, which assumes additive Drude-type conductivities for all charged species present.[43] For suspensions containing negatively charged particles with their counter-ions and additional non-reacting 1 : 1 electrolyte, it reads:

$$\sigma = ne(\mu_{\rm P} + \langle\mu^{+}\rangle) + M(\langle\mu^{+}\rangle + \langle\mu^{-}\rangle) + \sigma_{\rm B} \tag{1}$$

here, we used the number of added micro-ions of species i per particle, $M_i = n_i/n = c\ 1000\ N_A/n$ and the arithmetic means of all cationic (+), respectively anionic (−) micro-ionic mobilities:

$$\langle\mu^{+}\rangle = \frac{\sum_{\rm i} \mu_{\rm i} M_{\rm i}^{+}}{\sum_{\rm i} M_{\rm i}^{+}} \tag{2a}$$

$$\langle\mu^{-}\rangle = \frac{\sum_{\rm i} \mu_{\rm i} M_{\rm i}^{-}}{\sum_{\rm i} M_{\rm i}^{-}} \tag{2b}$$

The sums run over all ionic species present including $Z_{\rm bare}$ dissociated counter-ions. Particle mobilities were measured independently and mobilities of micro-ions were taken from the literature [$\mu_{\rm P} \approx (2\text{–}5.5) \times 10^{-8}$ m^2 s^{-1} V^{-1}, $\mu_{\rm H^+} = 36.23 \times 10^{-8}$ m^2 s^{-1} V^{-1}, $\mu_{\rm OH^-} = 20.52 \times 10^{-8}$ m^2 s^{-1} V^{-1}, $\mu_{\rm HCO_3^-} = 4.61 \times 10^{-8}$ m^2 s^{-1} V^{-1}, $\mu_{\rm Na^+} = 5.19 \times 10^{-8}$ m^2 s^{-1} V^{-1}, $\mu_{\rm Cl^-} = 7.91 \times 10^{-8}$ m ^{2}s^{-1} V^{-1},[89]]. The background concentration of micro-ions, $\sigma_{\rm B}$, is composed of contributions from water hydrolysis, from residual ions, *e.g.*, leaking from the container walls, and from partially dissociating CO$_2$. In deionized, decarbonized water, the contribution to the micro-ionic concentration from auto-dissociation is $c \approx 2 \times 10^{-7}$ mol L^{-1}, yielding $\sigma_{\rm H_2O}$ = 55 nS cm^{-1}. This contribution is important in systems of very small *n*.[58] The level of unidentified small ions typically does not exceed $c \approx 10^{-8}$ Mol L^{-1},[90] and its conductivity contribution can usually be neglected. However, suspensions equilibrated against ambient air contain small amounts of carbonic acid, and we use $\sigma_{\rm CO_3H_2} = 3.16$ μMol L^{-1} 1000 N_A e ($\mu_{\rm H^+} + \mu_{\rm HCO_3^-}$).

These values correspond to a concentration of carbonic acid of This approach allows a comprehensive charge characterization in terms of the number of surface groups N from conductometric titration, the number of dissociated groups $Z_{\rm bare}$ from the addition of neutral salts and the number effective conductivity charges Z_σ from density dependent conductivity measurements.

Photometric pH-measurements

For suspensions containing additional CO$_2$, $\sigma_{\rm B}$ in eqn (1) depends on the concentration of its reaction products. We therefore simultaneously determine the suspension pH, either using commercial equipment [electrode Sentix®81 with bridge pH/Cond 3320, WTW, Germany], or employing a newly developed photometric method.[76,83,91] Here, a spectrometer (AvaSpec, Avantis) samples the transmission spectra $I_T(\lambda)$ from which the adsorption ratio of two wavelength regimes in the blue and red is calculated (λ_1, λ_2, marked grey in Fig. 1c). Having calibrated the ratio against pH [using diluted universal indicator solutions (pH 3.0–10.0 indicator solution, Sigma-Aldrich, Germany) added to standard buffer solutions of pH between 3.0 and 8.0 (Merck, Germany)], the sample pH can be determined with an uncertainty of ±0.1 pH-units. For DI water containing increasing amounts of CO$_2$, Fig. 1e shows the obtained correlation between pH and conductivity (open diamonds). For performance checks, the conductivity can also be

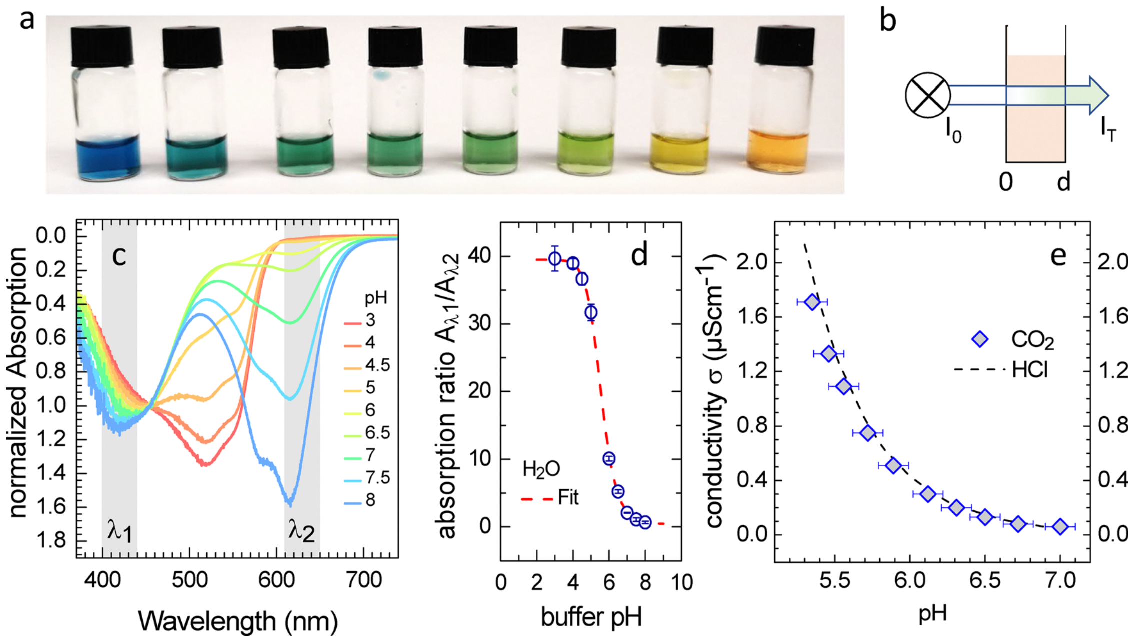

Fig. 1 Photometric pH determination. (a) Buffer solutions with indicator fluid. pH decreases from left to right. (b) Sketch of the set-up. (c) Absorption spectra normalized to the isobestic point for different pH values as indicated in the legend. The grey shaded regions indicate the two wave length ranges in the blue and red spectral region selected for evaluation. (d) Calibration curve: Absorption ratio $A_{\lambda_1}/A_{\lambda_2}$ as a function of adjusted pH. Data in (c) to (d) taken from ref. 83. (e) Performance check: correlation between pH and conductivity for the stepwise addition of CO$_2$ (Symbols) and of HCl (dashed line).

calculated using the aqion-freeware. The dashed line represents calculations made for the addition of HCl. We observe an overall good agreement between the two curves, except for a small but systematic difference, best visible at large amounts of added acids. The conductivities of the carbonized system show lower values. This can be attributed to the slightly larger phoretic mobility of the chloride ion.

In both experiments, care has to be taken to perform pH readings only on fully equilibrated and homogenized samples. Since conductivity and pH are determined in different positions (*cf.* Fig. S1 of the SI), and, moreover, the indicator shows a finite reaction time, one has to allow for a sufficient time interval between any stepwise changes in the sample composition and measurement (With a circuit volume of *ca.* 100 mL this may take up to a few a few minutes). Further, the electrode diaphragm of conventional experiment was often observed to slowly leak ions at non-negligible quantities. This standard method therefore requires much care during long-duration measurements in ultra-low salinity samples. The alternatively developed photometric approach does not interfere with the sample chemistry even over several hours. There, however, an important limitation is given by sample turbidity. In the presence of tracer particles, it performs well only up to the strong multiple scattering limit here found at $n \leq 6 \times 10^{17}\ \mathrm{m}^{-3}$ (the conventional method can be used up to $n \leq 3 \times 10^{19}\ \mathrm{m}^{-3}$, where its reproducibility becomes low). Below the threshold, pH-readings from photometry and conventional equipment agree within statistical uncertainty.

Super heterodyne laser Doppler velocimetry (SH-LDV)

SH-LDV is a now well-established technique for simultaneous studies of electro-phoretic mobilities of suspended particles and the electro-osmotic mobility at the container-walls.[57,73,79] It combines standard LDV[92–95] with the integral approach of Palberg[96] and the super-heterodyne configuration introduced to light scattering by Miller and Schätzel[97,98] and independently by Tanaka and Sonehara.[99] Measuring at small angles, it collects incoherently scattered light[100] and is therefore independent of the system structure.[56,58] Large particles and/or at elevated concentrations lead to a pronounced decrease in sample transmission by multiple scattering (MS).[80] To cope with that issue and to extend the range of accessible particle densities, we improved the original instrument and the data treatment.[58] Finally, using a sample cell with exchangeable side walls allows simultaneous investigations of up to three different surface types.[81] For further experimental details of SH-LDV, the reader is referred to the SI.

Fig. 2(b) shows typical Doppler spectra in the presence of MS. After applying an empirical correction (Fig. 2(c)), the spectra are evaluated for electrokinetic velocities and particle effective diffusivity by fitting expressions as derived in heterodyne light scattering theory [Fig. 2(d) and (e); see SI for further details]. Fig. 2(f) compares the particle concentration dependent mobilities for two model surfaces. The carboxylate stabilized polymer particles show a flat mobility maximum at intermediate concentrations and a value of $-5.2\ (\mu\mathrm{m\ s}^{-1})/(\mathrm{V\ cm}^{-1})$. The fused silica displays mobilities on the order of $-8\ (\mu\mathrm{m\ s}^{-1})/(\mathrm{V\ cm}^{-1})$ with no significant variations. The structure of the colloidal suspension is indicated by capital letters with F denoting a fluid and C denoting the crystalline state. Note that for technical reasons, no electroosmotic mobilities can be obtained in the latter state.[101] We further emphasize that the present electrokinetic measurements on latex spheres were performed at a constant number density which was located in the region of increasing mobilities of Fig. 2(f). The obtained mobilities are further evaluated for ζ-potentials and effective charges using an adaptation of the Standard Electrokinetic Model (SEM).[34,53]

Mean field calculations

As before, we utilize Poisson–Boltzmann (PB) theory within the cell-model approximation[102] to obtain theoretical estimates of electrostatic potentials Ψ and charges. In the following, we recap the main features of this approach used in ref. 84; for full details the reader is referred to the earlier publication. In the cell model, we approximate the colloidal solution of volume fraction Φ by a single colloidal particle (radius a), which is centered in a spherical cell (radius $R = a\ \Phi^{-1/3}$). To maintain a well-defined bulk value of the pH, the cell is grand-canonically coupled to a reservoir. We solve the one-dimensional PB equation in radial coordinates $r \in [a, R]$,

$$\left(\frac{\mathrm{d}^2}{\mathrm{d}r^2} + \frac{2}{r}\frac{\mathrm{d}}{\mathrm{d}r}\right)\Psi(r) = {\kappa_0}^2 \sin h(\Psi(r)) \tag{3}$$

to obtain the electrostatic potential Ψ and the distributions of ions within the cell. The Debye screening parameter of the reservoir, $\kappa_0 \equiv \sqrt{8\pi\lambda_\mathrm{B} n_0}$, is determined by the Bjerrum length $\lambda_\mathrm{B} = e^2/(4\pi\varepsilon_0\varepsilon_\mathrm{r}\ k_\mathrm{B}T)$ and the density n_0 of small ions (H^+, OH^-, Na^+, Cl^-) in the reservoir. For the salt free systems considered in the following, n_0 is calculated *via* the pH-value of the reservoir:

$$n_0 = \max\left(10^{-\mathrm{pH}_\mathrm{res}}, 10^{-(14-\mathrm{pH}_\mathrm{res})}\right)\mathrm{mol\ L}^{-1}\ N_\mathrm{A} \tag{4}$$

To obtain a mathematically well-defined problem, the PB equation has to be supplemented with suitable boundary conditions at the cell boundary ($r = R$) and at the surface of the colloidal particle ($r = a$). At the cell boundary, we use the Neumann boundary condition, $\Psi'\ (R) = 0$, to enforce global electroneutrality of the colloidal suspension. The surface of the colloidal particle contains weak, *i.e.*, pH-responsive groups, which are modeled by combining the Henderson–Hasselbalch equation for the average degree of dissociation, α, with the self-consistent charge regulation boundary condition introduced by Ninham and Parsegian.[103] Because this approach does not model electrostatic interactions between the surface groups,[104,105] the pK_a-values calculated using our theory thus have to be interpreted as "effective" pK_a-values that (approximately) contain the effect of inter-surface electrostatic interactions. The PB equation is solved numerically using SciPy,[106] effective charges are calculated from the numerical solutions using the analytical method of Trizac *et al.*[107]

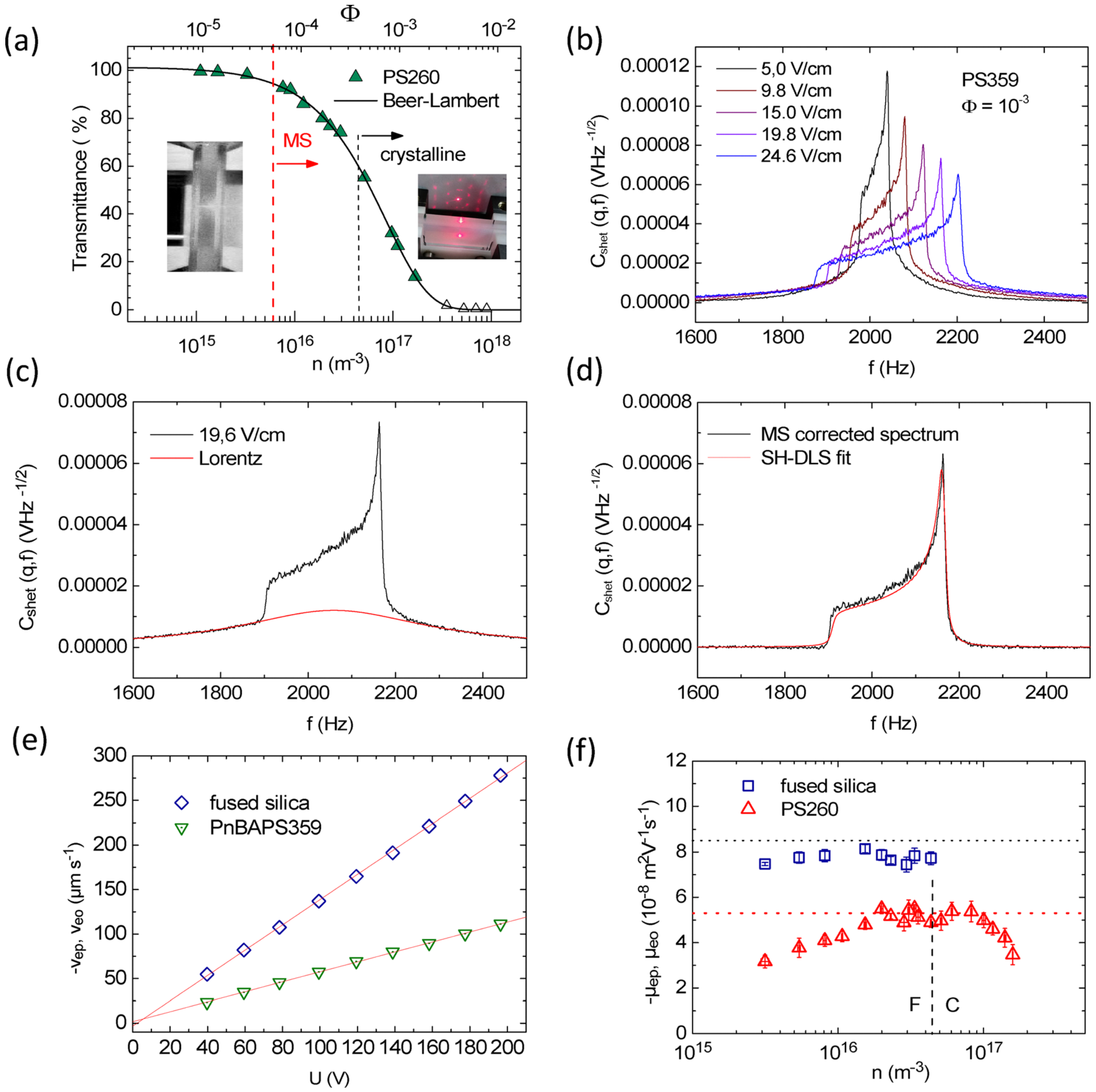

Fig. 2 SH-LDV experiments. (a) Typical dependence of the transmittance on particle concentration for a suspension of polymer latex particles of 260 nm diameter. The upper scale gives the volume fraction, while the lower scale denotes the number density, which are related by $\Phi = n\,(4\pi/3)\,a^3$. The solid line denotes a fit of Beer–Lambert law. For the shown suspension, multiple scattering occurs for $n > 6 \times 10^{15}$ m^{-3}, *i.e.* at ∼95% transmission (dashed red line and left inset). For $n > 4 \times 10^{16}$ m^{-3}, the suspension crystallizes (blue short-dashed line and right inset). (b) Field-strength dependent SH-LDV spectra. (c) Spectrum with MS-background, which is well described by fitting a Lorentzian to the regions right and left of the main spectral feature (solid red curve). (d) the same spectrum after subtraction of the MS background. The solid line is a least-squares fit of the theoretical SH-LDV spectrum with three independent fit parameters: solvent velocity at the wall, v_{eo}, particle velocity, v_{ep}, and particle effective diffusivity D_{eff}. (e) Field-strength dependent velocities extracted from fitting. Least-squares fits of linear functions yield the respective mobilities of wall and particles, $\mu = v/E$. (f) Comparison of the characteristic number density dependence of experimental mobilities of a fused silica and a polymeric surface, both in contact with deionized and decarbonized water. The error bars correspond to the standard error of the fits to the Doppler-spectra at a confidence level of 0.95. Dotted lines are guides to the eye. Data in (a) to (e) taken from ref. 80. Data in (f) taken from ref. 58.

Molecular dynamics simulations

Silica slabs with variable surface chemistry and an adjustable degree of ionization were created as supercells from the unit cell of the α-cristobalite crystal structures.[108] The Q4 surface is uncharged and silanol-free, while the Q3 surface in addition carries silanol groups with a density of 4.7 nm^{-2}. A hydrophobic organic surface was created as a supercell from the experimentally resolved L-isoleucine crystal.[109] The box dimensions for the silica Q4 system were $(3.168 \times 3.308 \times 16.368)$ nm^3 while for Q3 the cell geometries are $(3.340 \times 3.487 \times 13.371)$ nm^3, respectively, and 3D periodic boundary conditions were applied. Slab structures were placed in the center of the simulation box with a single face exposed to the solvent. 50 molecules of CO_2 and, where applicable, salt ions were randomly added and the remaining box volume filled with water molecules. Water was described by the TIP3P model.[110] Ion–ion interactions were accounted for using the standard

CHARMM27 force field,[111,112] while CO_2 parameters were taken from ref. 113.

Simulations were carried out in the canonical ensemble, where the velocity-rescaling thermostat[114] with a relaxation time of 0.1 ps, was used to control the temperature. A time step of 1 fs was set to update atom positions and velocities. For non-bonded interactions, a pair list was created with a cut-off radius of 1.4 nm and updated after every 10 fs. The cut-off for the shifted Lennard-Jones potential was set to 1.2 nm. For the long-range electrostatic interactions, the Particle Mesh Ewald-Switch method[115] was used with a Coulomb switching cut-off 1.2 nm. To truncate the Van-der-Waals interactions, a dispersion correction was applied. A short 1 ns semi-isotropic NPT simulation was performed to equilibrate the solvent density, where we employed a Parrinello–Rahman barostat.[116] After the equilibration, all the production simulations were extended up to 100 ns.

Results

In this section, we present an overview of the most important effects of molecular CO_2 quoted from our previous study and obtained in the present investigation. We start with the experimental observation of (i) the de-charging of weakly acidic surfaces, (ii) the recharging of de-charged surfaces upon the addition of salts and (iii) the enhanced charging of nominally inert hydrophobic oxide surfaces. We then turn to the results of our simulations regarding the adsorption of molecular CO_2 at all investigated surfaces and the effects this has on the ionic structure of the EDL. Together, this will allow the development of a consistent description of the opposing effects molecular CO_2 has on surface charge in terms of a local enhancement of interactions directly and indirectly related to electrostatics.

CO_2-induced decharging and suppression of counter-ion exchange

Conductometric charge characterization yields access to all relevant charges of colloidal particles. Comparing experiments in two salt-free states, *i.e.*, decarbonized and equilibrated against ambient air, shows the effects CO_2 has on these charges.[84] Fig. 3a compares the background-corrected number density-dependent conductivities of PnBAPS359 suspensions for these two states. In both cases, we observe a linear increase as known from literature[43] and expected from eqn (1) for $M = 0$. Fitting linear functions to the data we obtain the effective conductivity charge as $Z_\sigma = (2.35 \pm 0.04) \times 10^3$ and $Z_\sigma = (1.30 \pm 0.07) \times 10^3$, in the decarbonized state and after equilibration with ambient air, respectively. The number of freely moving counter-ions halves in the presence of CO_2.

Fig. 3(b) compares the background- and particle contribution-corrected conductivities per particle for the two states in dependence on the number of micro-ions added per particle. In the decarbonized state (black circles), the data first increase steeply. In fact, they initially follow the expectation for the conductivity contribution per particle of HCl (dash-dotted line). The curve then bends over and runs parallel to the expectation for the conductivity contribution of CsCl (short-dashed). This behavior indicates an exchange of initially present H^+ for the added cation.[43] Starting with a deionized suspension equilibrated to ambient air, we only observe a strictly linear increase (blue diamonds) following the expectation for the conductivity contribution of CsCl. Thus, there is no ion exchange. Least squares fits of eqn (1) and (2) with n, Z_σ and M as input yield bare charges of $Z_{\text{bare}} = (9.92 \pm 0.05) \times 10^3$ and $Z_{\text{bare}} = (1.34 \pm 0.06) \times 10^3$ for suspensions without and with CO_2, respectively. For comparison, we had $N = (134 \pm 2) \times 10^3$ from conductometric titration. We stress, that charge numbers derived from

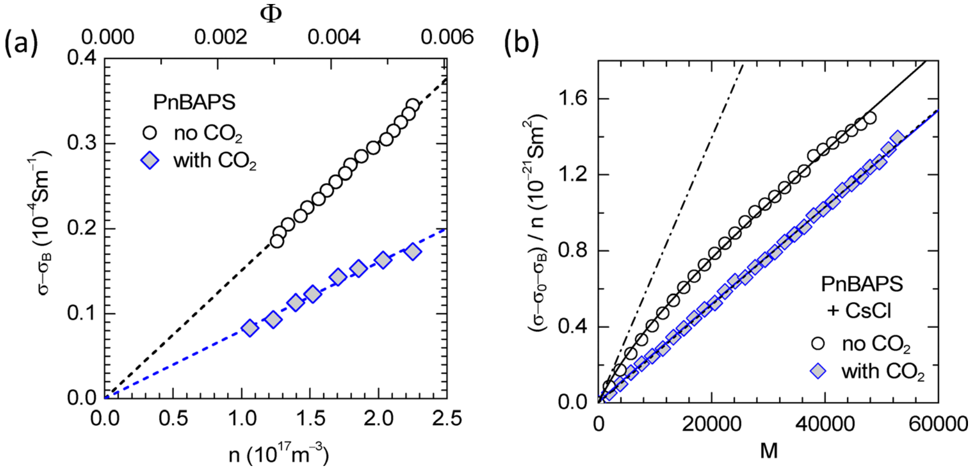

Fig. 3 Conductometric charge characterization and counter-ion exchange. (a) Background-corrected conductivities as a function of number density n for the two representative conditioning states as indicated in the key. The upper scale shows the volume fraction, $\Phi = (4/3)\pi a^3 n$. The dashed lines are least squares fits of eqn (1). Data taken from ref. 84. (b) Background- and particle contribution-corrected conductivities per particle in dependence on the number of added micro-ions per particle for the two representative states as indicated in the key. The dash-dotted and dashed lines are the theoretical expectations for the conductivity contribution of added HCl and CsCl, respectively. The solid lines are least squares fits of eqn (1) and (2) to the data. Data taken from ref. 84.

experiments using different alkali halides like LiCl, NaCl, KCl, KBr *etc.* agree quantitatively.[84] The presence of CO_2 thus acts directly on the state of dissociation of the weakly acidic surface groups.

Discrimination of an additional decharging effect

Different effects at work in decharging can be discriminated by monitoring the ζ-potential upon adding different non-reacting electrolytes.[83] Always starting from a deionized and decarbonized state, NaCl, respectively HCl-solutions were added successively to the suspension; for CO_2 we increased its concentration in the reservoir atmosphere up to $\approx$90% CO_2 and cycled the suspension, until equilibration was obtained. In Fig. 4(a) and (b), we compare the electrophoretic behavior of the hydrophilic surface to that of the hydrophobic surface as was observed in ref. 83. We plot the measured ζ-potentials *versus* the total micro-ion concentration, both normalized to the reference values in the deionized and decarbonized state. For the addition of CO_2, ambient conditions are marked by the red arrow. In all cases, we observe a linear decrease with the logarithm of the total ion concentration. For the hydrophilic surface stabilized by hydroxyl groups [Fig. 4(a)], we observe NaCl to induce a weak decrease caused by screening effects. The same effect is also observed for other chloride salts (not shown). Adding HCl, the slope steepens, as now aditional pH-driven charge regulation occurs. Screening and charge regulation are also expected upon equilibration with CO_2 due to its dissociation products. Upon the addition of CO_2, however, the slope still steepens further. Thus, we observe decharging well beyond the expected effects of screening and pH-driven charge regulation. This demonstrates an additional decharging mechanism that must be related to molecular CO_2.

For the polymeric surface [Fig. 4(b)], the effect of pH-driven charge regulation is less pronounced due to the different surface chemistry. However, here the addition of CO_2 leads to a drastic decharging in line with the observations from conductivity. Note that we have near complete decharging after equilibration against an almost pure CO_2 atmosphere. In fact, experiments using a pure CO_2 atmosphere led to the onset of coagulation. As can be seen, all additives lead to decharging. As expected the relative decharging depends on the type of surface and the type of additive. Remarkably, however, for both hydrophilic and hydrophobic surfaces, the CO_2-related combined effects significantly surpass that observable for screening alone, respectively for screening plus pH-driven charge regulation.

CO_2 induced shifts of the dissociation equilibria

Our findings were cross-checked and rationalized in ref. 84 by Poisson–Boltzmann cell model (PBC) calculations under charge regulating boundary conditions. We calculated the bare charges for a fixed volume fraction of $\Phi = 4 \times 10^{-3}$ of PnBAPS particles using their titrated surface group number $N = 134 \times 10^3$, and a variable surface pK_a as input. The results for Z_{bare} are shown in Fig. 5(a) as solid lines in dependence on the chosen surface pK_a. Since Z_{bare} and Z_{PBC} depend on the amount of EDL overlap, and thus on n,[37,117] we subsequently performed additional calculations under variation of the volume fraction. The range of bare charges obtained under variation of the number density of particles between $n = 10^{16}\ m^{-3}$ and $n = 10^{17}\ m^{-3}$ is included in Fig. 5(a) as light shaded region. At pH 7, the order of magnitude variation in n translates to a $\approx$2% variation of Z_{bare}. The experimentally observed bare charge is recovered for a surface pK_a of 4.26, (dotted vertical line). This is compared to the results obtained under ambient CO_2 conditions (orange solid line, pH = 5.5). In this case, one would expect a bare charge of $Z_{bare} \approx 6 \times 10^3$ given an unchanged surface pK_a. Now, however, the experimentally observed bare charge is recovered for a surface pK_a of 6.5. Note that these values show a negligible dependence on particle concentration.

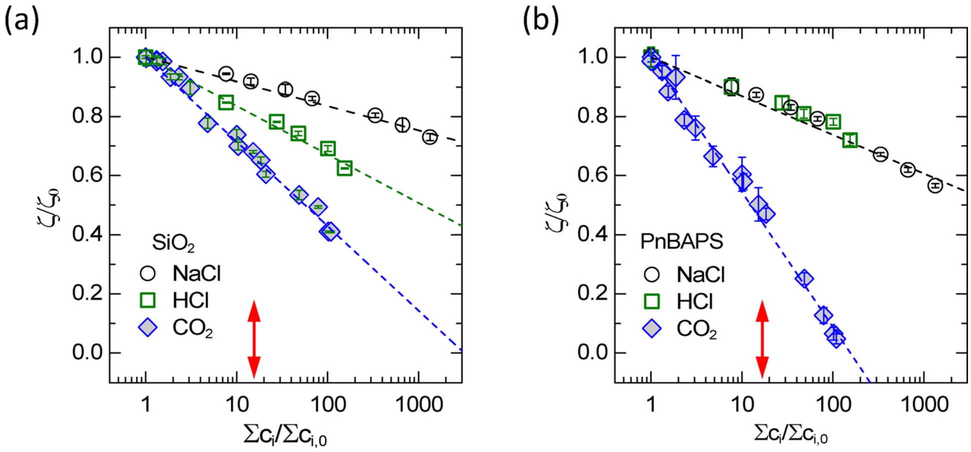

Fig. 4 Discrimination of decharging effects. Measured ζ-potentials *versus* the total micro-ion concentration, both normalized to the reference values in the deionized and decarbonized state. (a) Data for a fused silica surface upon adding three different kinds of chemicals as indicated in the key. The error bars correspond to the standard error at a confidence level of 0.95 of the fits to the Doppler-spectra. Dashed lines are least squares fits of eqn (1) to the data. For orientation, the red arrow denotes the total microion concentration obtained upon equilibration of salt free suspensions against ambient air. (b) Same as (a) but for the polymeric surface. Data taken from ref. 83.

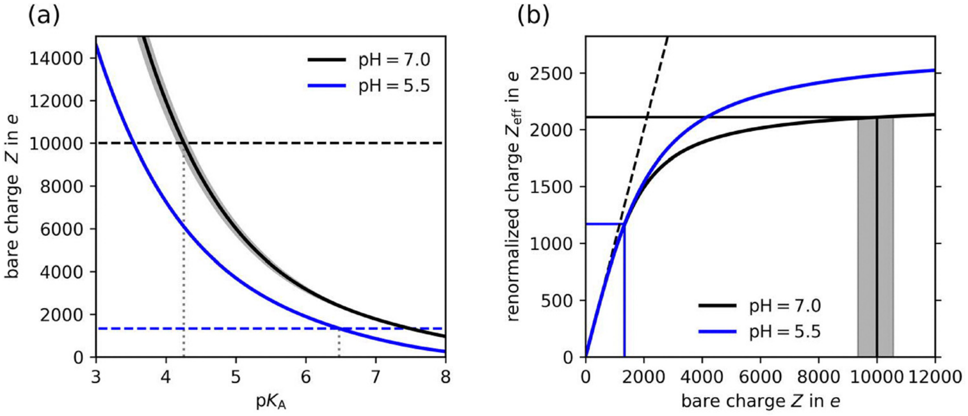

Fig. 5 Results from cell-model calculations. Comparison of data obtained using the Poisson–Boltzmann cell-model for the salt and CO_2-free state at pH_{bulk} = 7 (black) and the CO_2-equilibrated state at pH_{bulk} = 5.5 (blue). (a) Bare colloidal charges calculated for different surface group pK_a-values (solid lines). For pH = 7 the grey shaded regions indicate the variation of Z_{bare} due to its dependence on n. The variations are even less significant at pH = 5, in fact so small that the shaded region is hidden by the line thickness. The experimentally observed bare charges are shown as dashed horizontal lines; crossing points with the curves obtained from the PBC allow to estimate effective surface pK_a-values of 4.26 and 6.5, respectively. (b) Renormalized charge as a function of the corresponding bare charge. The hypothetical case without charge renormalization ($Z_{PBC} = Z$) is shown as a black dashed line.

Fig. 5(b) compares the numerically obtained effective charges, Z_{PBC}, for both considered pH-values as a function of the bare charge. While for small bare charges both curves collapse onto $Z_{PBC} = Z$, as the bare charges increase, they bend over, indicating substantial charge renormalization. In qualitative agreement with the results of Alexander *et al.*,[117] the saturation value at the increased salinity obtained in the presence of CO_2 is larger than in its absence. Note that the small variation in Z_{bare} due to its dependence on n (shaded regions) translate to an even smaller variation in Z_{PBC}. At pH_{bulk} = 7.0, where we had $Z_{bare} = (9.92 \pm 0.05) \times 10^3$ and $Z_\sigma = (2.35 \pm 0.04) \times 10^3$, the theory predicts a value of Z_{PBC} = 2100. For pH_{bulk} = 5.5, where we had and $Z_{bare} = (1.34 \pm 0.06) \times 10^3$ and $Z = (1.30 \pm 0.07) \times 10^3$, the theory predicts a renormalized charge of Z_{PBC} = 1170. For both pH values, the theoretical predictions deviate less than 10% from experimental values and are thus in reasonable agreement. As in the experiments, the decrease of the bare charge is mirrored by the accompanying decrease of the renormalized charge. Further note that variations of Z_{bare} due to an altered colloid density n do not translate to appreciable variations of Z_{eff}. Moreover, at pH = 7 there is a large difference between the bare and the renormalized charge, which is absent at pH = 5.5. Consequently, hardly any counter-ions are left for exchange, which explains the experimental observations of Fig. 3(b).

For the silica surface, we give estimates of the isoelectric points (I.E.P.) from a plot of measured ζ-potentials as a function of pH. Data in Fig. 6 arrange in two groups corresponding to the two different conditioning states.

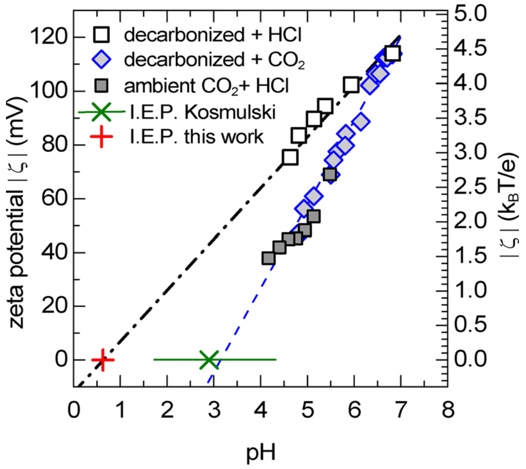

Fig. 6 Estimating the I.E.P. of fused silica surfaces. Magnitudes of ζ-potentials in dependence on suspension pH for three different cases indicated in the key. The dashed line is an extrapolation towards vanishing ζ-potential corresponding to the isoelectric point yielding $pH_{I.E.P.} \approx 3.1 \pm 0.1$. Green Symbols are data as reviewed by Kosmulski.[86] The green cross denotes the median of a sub-sample as collected by Parks,[85] while the green bar denotes the spread of literature values for silica not included therein. The open symbols denote the potentials upon addition of acid to a system in the strictly CO_2-free state. The dash-dotted line is a linear extrapolation towards the I.E.P. under decarbonized conditions (red cross) yielding $pH_{I.E.P.} \approx 0.6 \pm 0.3$.

The data obtained for adding HCl under ambient conditions (*cf.* Fig. 7 below) superimpose with the data obtained for adding CO_2 to a decarbonized system [*cf.* Fig. 4(a)]. The combined data extrapolate to zero potential at approximately pH ≈ 3.1. Notably, this value is in good agreement with the average value reported by Parks for measurements taken without special precaution to exclude CO_2 ([85] green cross in Fig. 5) and also well inside the range reported in Kosmulski's more recent data compilation ([86] green bar in Fig. 6). In stark contrast, for the data obtained for the addition of HCl to a decarbonized system (*cf.* Fig. 4(a) and 7 below), the same linear extrapolation leads to a pH-value significantly below 1. While we are aware of the limited precision of such extrapolations in particular for silica, our result nevertheless might imply a significant qualitative

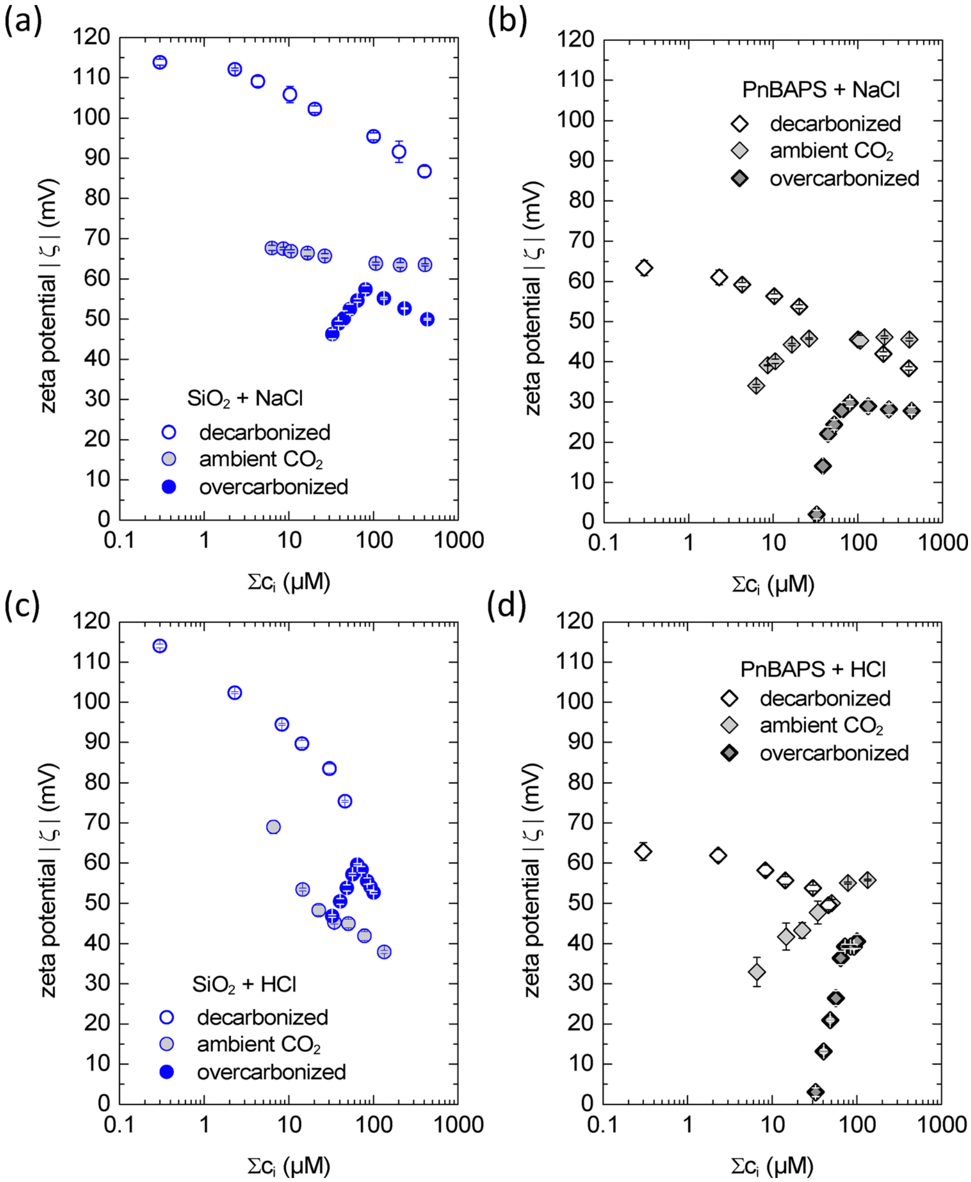

Fig. 7 Interplay of decharging and recharging processes in dependence on CO$_2$ content. Semi-logarithmic plots of the magnitudes of ζ-potentials in dependence on total micro-ion concentration for SiO$_2$ (blue) and PnBAPS (black). The error bars correspond to the standard error at a confidence level of 0.95 of the fits to the Doppler-spectra. (a) Data taken for the silica surface upon the addition of NaCl starting from different state as indicated in the key. (b) The same, but for PnBAPS. (c) Data taken upon addition of HCl starting from different state as indicated in the key. (d) The same, but for PnBAPS. Data were recompiled from ref. 82 and 83.

reduction of the I.E.P., if molecular CO$_2$ is strictly excluded from the systems under study. Since the I.E.P. is largely determined by the presence respectively absence of dissociated hydroxyl groups, the shift in the I.E.P. indicates a corresponding increase of the degree of dissociation. This is in line with the above discussion of the polymeric surface. Together, our analysis suggests that both the lowering of bare charge numbers at the polymer surface and the I.E.P. shift at the mineralic surface can be viewed on a common footing: *i.e.*, a dependence of the dissociation equilibrium of weakly acidic surface groups on the amount of molecular CO$_2$ present in the system.

The Janus-nature of CO$_2$

Above we studied the charge state of hydrophobic and hydrophilic model surfaces under the addition of simple 1 : 1 electrolytes, *i.e.* NaCl and HCl. In four experimental series, we now explore how the observed behavior is further modified by the presence of CO$_2$ and summarize our results in Fig. 7.[82,83] We focus on three different background levels of CO$_2$: decarbonized, equilibrated to ambient air and equilibrated against a nearly pure CO$_2$ atmosphere.

Adding NaCl addresses the combined influence of screening and CO$_2$. In the semi-log plots of Fig. 7(a) and (b), we consider the addition of pH-neutral electrolyte (NaCl). We show the moduli of the measured ζ-potentials as a function of total micro-ion concentration. Both potentials are, of course, negative due to charging by carboxylate, respectively hydroxyl groups. For the fused silica surface under ambient conditions, we observe a near linear decrease, which, however, is less steep than without CO_2 [Fig. 7(a)]. At over-carbonized conditions, we observe a mobility maximum with a peak value of 60 mV. While the ascent is quite steep, the descent shows a slope rather similar to that observed in the decarbonized state. For the polymer surface [Fig. 7(b)], the linear decrease with increasing logarithm of the total micro-ion concentration switches to an increase followed by a very weak decrease already at ambient conditions. Under over-carbonized conditions, we find an even steeper increase followed by a slightly steeper, albeit still weak decrease.

In Fig. 7(c) and (d), we compare both surfaces under the addition of a strong acid, where under decarbonized conditions we saw the combined action of screening and pH-driven charge regulation. For the silica surface, [Fig. 7(c)], we observe a slightly steepening, respectively a slightly flattening decrease both in the decarbonized state and under ambient conditions. However, a sharp and pronounced maximum occurs upon addition of HCl in the over-carbonized state, again with a peak value of $\zeta \approx -60$ mV. In contrast, at the polymeric surface, [Fig. 7(d)], we observe a decrease under decarbonized conditions but an increase already under ambient conditions. At over-carbonized conditions, we observe a still steepened increase.

We emphasize that in all runs the covered ranges of pH and salinity are well comparable. The decisive difference is the presence or absence of CO_2. In the presence of dissolved CO_2, we see a transition from decharging to (transient) recharging for stepwise increasing CO_2 content in all four series. This contrasts with the observations in the decarbonized state, where we only see decharging. As before, the expected effects for the dissociation products of CO_2 are the same as for HCl in decarbonized systems. We may therefore conclude that the differences observable after equilibration against CO_2-enriched atmospheres are due to the presence of molecular CO_2.

Our experiments using combining different surfaces with different electrolytes under well controlled CO_2 concentrations again reveal the Janus nature CO_2 in its influence on the different processes of charge adjustment. Moreover, it points to an additional charging mechanism not yet considered. While that mechanism appears to be absent under decarbonized conditions it becomes rather pronounced and dominant at over-carbonized conditions. But specific differences are observable for the two surfaces and the two electrolytes. The maxima are much sharper in the case of silica and of similar height for the two electrolytes, while at the polymeric surface, the decrease is sluggish, if present at all. At the polymer surface the maximum observed values increase when moving from NaCl to HCl, despite pH-driven charge regulation. However, no clear maxima emerge for the range of HCl-concentrations probed. This may suggest that in the latter case recharging continues in parallel to decharging of the weakly acidic surface groups. Comparison to existing reports on potential maxima[61–63] suggests co-ion adsorption as a possible candidate for the recharging mechanism.

Co-ion adsorption

We pursue this suggestion by determining the ζ-potential under addition of sodium salts from the lyotropic series NaF, NaCl, NaBr, and NaI. We compare the two different model surfaces at decarbonized and ambient CO_2 conditions in dependence on the total micro-ion concentration and present the results in Fig. 8.

For the decarbonized silica surface in Fig. 8(a), we see a linear decrease irrespective of the co-ion species. Data for the larger ions coincide, while the data for NaF show a slightly steeper slope. This decrease corresponds to the expected effects of increased screening with increasing salt concentration. Under ambient CO_2 conditions, the decrease has weakened for NaF and NaCl, while it has turned to an increase for the larger co-ion species [Fig. 8(b)]. The identical behavior is observed in Fig. 8(c) for the polymer surface already under decarbonized conditions. Here, the maximum ζ-potentials exceed the potential of the decarbonized salt-free surface. Under ambient CO_2 conditions, all data collapse onto a single curve showing an initial increase followed by a plateau at a ζ-potential of approximately $\zeta \approx -45$ mV. This is of the same order of magnitude as reached for the same total concentration of small ions under addition of screening 1 : 1 chloride salts. This remarkable plateauing behavior observable for both surfaces points to an ongoing co-ion adsorption paralleled by a further increase in screening effects.

Fig. 8(d) shows a fascinating indifference of the position and shape of the maxima to co-ion type. This is similar to the findings reported in (ref. 3), where it was used as an argument against co-ion adsorption. Comparison of all four situations displayed in Fig. 8, however, clearly demonstrates that maximum occurrence depends both on co-ion type and surface type. Increased co-ion size and chaotropic character as well as an increased surface hydrophobicity favor the switch from decharging to recharging as seen in the increasing ζ-potentials. Remarkably, however, it also depends on the presence or absence of CO_2. We clearly recognize that the presence of CO_2 significantly supports the development of ζ-potential at both surfaces.

Charging of a chemically inert oxide

In this section, we compare the charge state of the sapphire (0001) surface immersed in salt-free water in the absence and in the presence of ambient CO_2. Fig. 9 shows a representative result for a buffer-free sample. In the decarbonized state at neutral pH, we observe a finite electroosmotic mobility of $\mu_{\text{sapphire}} = (-2.4 \pm 0.3)\ 10^{-8}\ \text{m}^2\ \text{V}^{-1}\ \text{s}^{-1}$. The surface carries a moderate negative charge. Upon adding CO_2, the mobility increases by about a factor of three to $\mu_{\text{sapphire}} = (-7.9 \pm 0.2)\ 10^{-8}\ \text{m}^2\ \text{V}^{-1}\ \text{s}^{-1}$. These values correspond to ζ-potentials

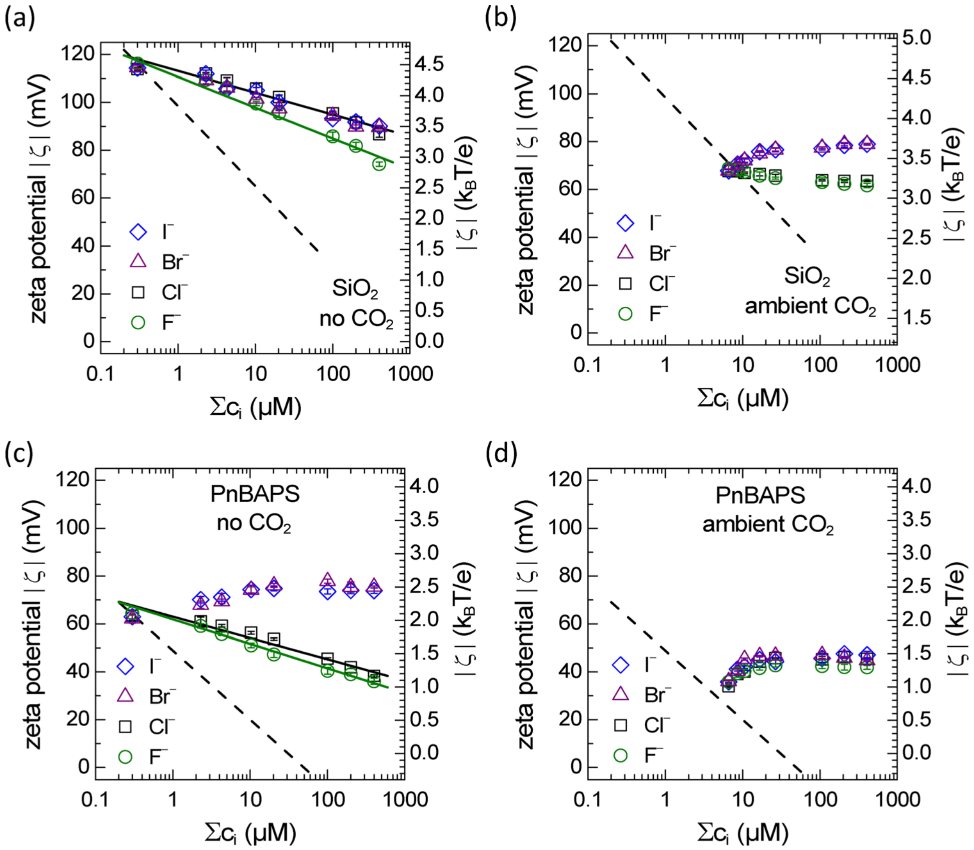

Fig. 8 Effect of adding Na-salts with different co-ions to differently conditioned hydrophilic and hydrophobic model surfaces. (a) Semi-log plot of the magnitudes of ζ-potentials of the fused silica surface in mV (left scale) and reduced units (right scale) in dependence on the total micro-ionic concentration for different salts as indicated in the key. The error bars correspond to the standard error at a confidence level of 0.95 of the fits to the Doppler-spectra. The dashed line shows for comparison the ζ-potential for the addition of CO$_2$ to salt-free systems. (b) The same but now after equilibration to ambient air. (c) The same for the PnBAPS surface in the decarbonized state. (d) The same for the PnBAPS surface at ambient conditions.

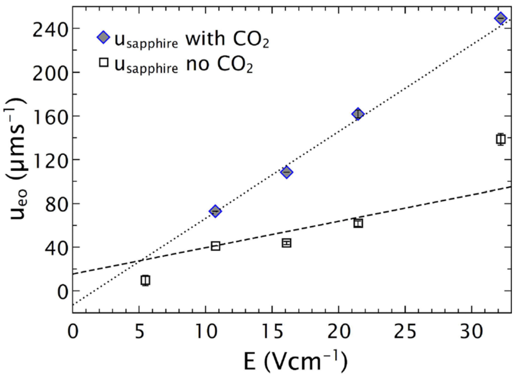

Fig. 9 Electroosmotic velocities at sapphire [0001]. We compare data taken in the decarbonized state (open circles) to data taken after equilibration to ambient air (shaded diamonds). The lines represent least squares fits of a linear function to the data and the error bars denote uncertainties of the fits to the spectra at a confidence level of 0.95. For the decarbonized and the equilibrated state, the slopes return mobility values of $\mu_{\text{sapphire}} = (-2.4 \pm 0.3)\ 10^{-8}\ \text{m}^2\ \text{V}^{-1}\ \text{s}^{-1}$ without CO$_2$ and $\mu_{\text{sapphire}} = (-7.9 \pm 0.2)\ 10^{-8}\ \text{m}^2\ \text{V}^{-1}\ \text{s}^{-1}$ at ambient conditions, respectively.

of −30 mV and −97 mV. In the literature, ζ potentials at this pH were reported for various types and concentrations of background electrolyte and buffers, as well as for different sample pretreatment and cleaning procedures.[118,119] Our result obtained at zero CO$_2$ lies at the lower bound of the reported range, the result obtained under ambient CO$_2$ conditions exceeds this range at its upper end. This supports the claim to CO$_2$-free conditions made for most of the studies.[118,119] We stress that the observed increase in ζ-potential upon the addition of CO$_2$ is opposite to what is expected for its dissociation products. This again suggests that molecular CO$_2$ takes an important role in the observed charge increase.

Further measurements under variation of CO$_2$ content, adjusted pH and concentrations of added simple electrolytes are clearly warranted for a more systematic picture. They are, in fact, under way and will be reported elsewhere. While in this sense preliminary, our comparison nevertheless clearly demonstrates that the presence of CO$_2$ at a chemically inert surface strongly assists the charging process ongoing at that surface in salt-free and pH-neutral water.

Simulation results

Previous investigations had indicated that at surfaces in contact with water containing molecular CO$_2$, the latter enriches in a diffuse layer close to the surface.[82] We now follow that issue

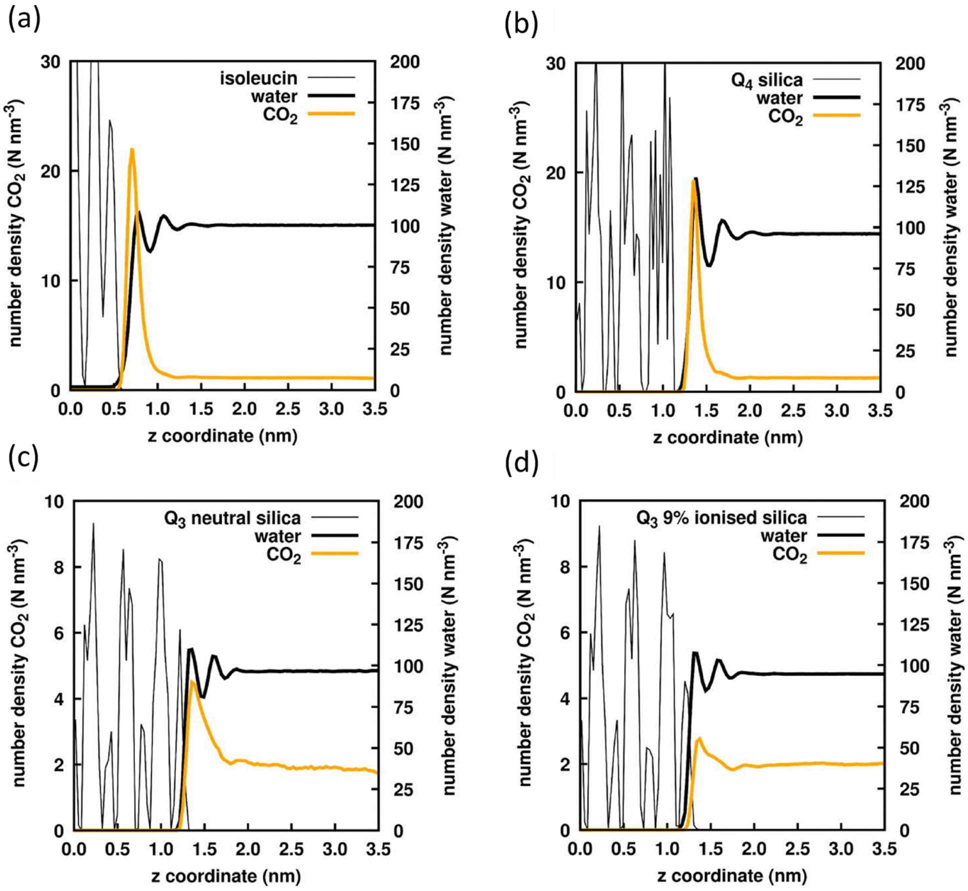

Fig. 10 Diffuse adsorption of CO_2 at various surfaces. Shown are the density profiles of water (thick black lines, right scale) and CO_2 (orange lines, left scale) at (a) uncharged Isoleucin, (b) uncharged Q4 silica; (c) uncharged Q3 silica, and (d) 9% ionized Q3 silica. The hydroxyl group density in the latter two cases was 4.7 nm^{-2}. The thin solid lines to the left show the densities of surface atoms.

systematically and in more detail. Fig. 10 shows the density profiles obtained for water and for a bulk concentration of 2 nm^{-3} CO_2 at four representative surfaces. Crystalline Isoleucin is an uncharged hydrophobic organic surface. The silica Q4 surface is an uncharged and hydrophobic mineral surface. The hydrophilic silica Q3 surface in addition bears ionizable hydroxyl groups. We here study it at zero and at 9% degree of deionization. At both hydrophobic surfaces, CO_2 enriches close to the surface with peak densities above and around 20 nm^{-3}. At Isoleucin, CO_2 fills the gap between the surface and the first water layer. At the silica Q4 surface, the water structure is very pronounced and the location of the CO_2 peak coincides with the first water layer. We stress that this enrichment does not imply any anchoring or attachment to the surface. Rather, the molecules retain their capability of free motion. Moreover, we do not see any indications of a preferred orientation. CO_2 enrichment is also seen at both hydrophilic surfaces; however, the effect decreases with increasing degree of dissociation. The location of the CO_2 peak shifts slightly outward in the presence of hydroxyl groups, but does not change upon their dissociation.

Next, we studied the dependence of the adsorbed amount on the concentration of a simple electrolyte, NaCl. Fig. 11(a) to (c) compares the densities of CO_2 at the three silica surfaces. In particular for the uncharged surfaces, the amount of stored CO_2 increases significantly as the concentration of salt is increased. Interestingly, neither the surface-specific water structure, nor the location of the CO_2 peak were found to move in the presence of salt. However, the presence of salt may influence the extent of CO_2 enrichment. At silica Q4, the CO_2 surface density now surpasses the bulk density by more than an order of magnitude. At the Q3 surface, the enrichment reaches 200% as compared to the bulk. For the partially ionized surface the effect is not that significant and the enrichment stays at roughly 50% of the bulk value. Note, however, that in all cases, the enrichment is observable out to the second water density minimum.

The presence of adsorbed CO_2 influences the structural arrangement of salt ions at the surface. This is shown in Fig. 12. At all surfaces, we see a more or less pronounced arrangement of the added ions in layers, with the first Na^+ layer lying closer to the surface than the first Cl^- layer. For both charge-neutral surfaces, co-ions and counter-ions are depleted from the immediate surface environment. This depletion effect is increased in the presence of CO_2. At silica Q4, the location of Na^+ density maxima correlates to the location of water density

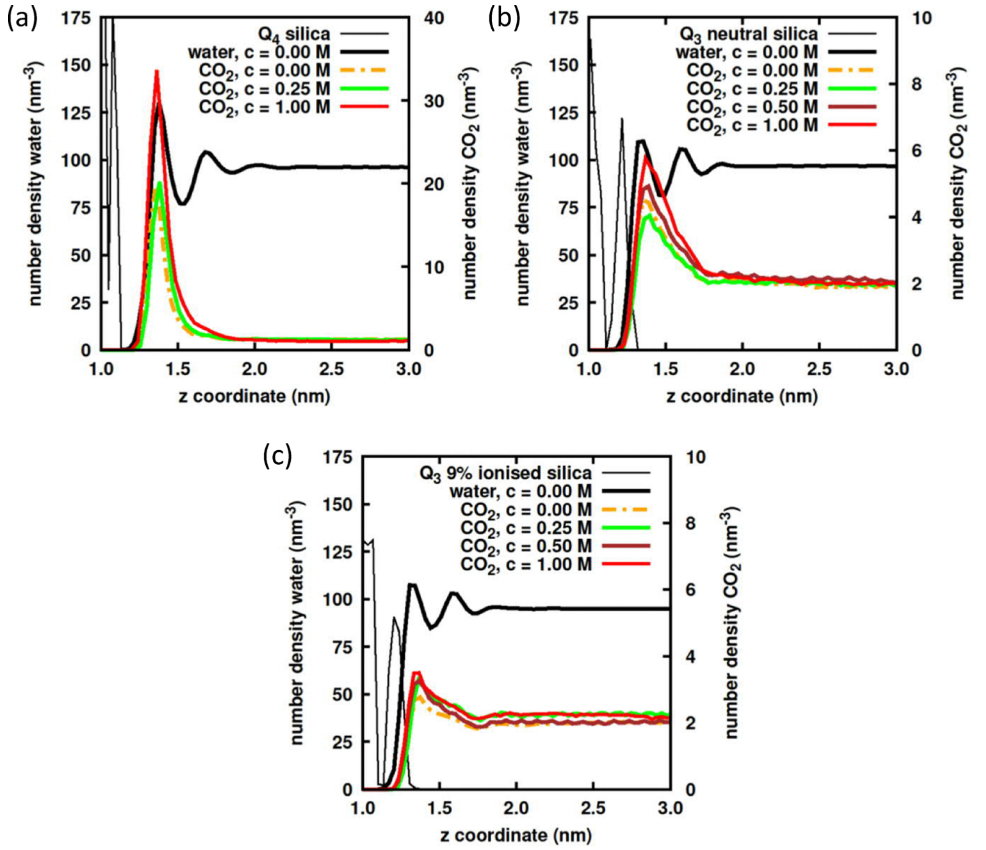

Fig. 11 Influence of salt on CO_2 enrichment. Shown are the density profiles of water (thick black lines, left scale), CO_2 (colored lines, right scale) at (a) uncharged Q4 silica, (b) uncharged Q3 silica, and (c) 9% ionized Q3 silica. The CO_2 line color denotes the background concentration of 1 : 1 electrolyte (NaCl) as indicated in the key. The thin solid lines to the left show the densities of surface atoms.

minima, while the Cl^- density maximum coincides with the second water maximum. The locations do not depend on the amount of CO_2 present. With CO_2, however, hardly any Cl^- structure is left. At the Q3 neutral surface without CO_2, the location of Na^+ density peaks is shifted outward as compared to Q4. In the presence of CO_2 this shift is still increased. Also for Cl^-, the presence of CO_2 causes an outward shift in the location of the density peak. For both ions, the structure is less pronounced in the presence of CO_2. Together, this demonstrates a competition between CO_2 and ions based on steric interactions.

By contrast, we find an enrichment of ions at the 9% ionized silica Q3 surface due to the now present electrostatic attraction of counter-ions to the surface and of co-ions to the counter.-ions. Interestingly, the location of the density peaks of both counter- and co-ions shifts closer to the surface in the presence of CO_2. The first peak maximum density of Na^+ increases significantly in the presence of CO_2, while it is slightly diminished in the second and third layer and in the bulk. Remarkably, also the first layer density for Cl^- increases strongly once CO_2 is present. Thus, at charged surfaces, CO_2 enhances the EDL structuring, and it increases the amount of surface enriched ions. Both issues point to an enhancement of electrostatic interactions due to the presence of CO_2 enriched in the innermost part of the EDL.

We next quantify the dependence of the salt ion structure on the bulk salt concentration in Fig. 13. For constant CO_2 concentrations, we compare the ion profiles for Na^+ (left) and Cl^- (right) for three increasing background salt concentrations. Interestingly, at the lowest salt concentration, the salt structure is only weakly pronounced and resembles that observed for the neutral Q3, *i.e.*, we see a weak overall enrichment of Na^+ and a weak overall depletion of Cl^- towards the surface. With increasing salt concentration, the density maxima for Na^+ become ever more pronounced with a slight inward shift of the maximum location. For Cl^-, the behavior is more complex. The density oscillations become progressively more pronounced. The overall depletion, which initially was visible out to about 2 nm is reduced., However, even at the largest salt concentration, the density at the first Cl^--peak still remains below that of the bulk, while at the dominant second peak, it significantly exceeds the bulk density. This changing balance between steric repulsion and electrostatic attraction upon increasing the salt concentration strongly suggests that the EDL ionic structure in the presence of CO_2 is clearly dominated by the electrostatic interactions. These give both rise to a prominent first counter-ion layer, which in turn induces a pronounced co-ion layering.

An interesting additional question relates to the degree of charge accumulation by the adsorbed 1st layer counter-ions.

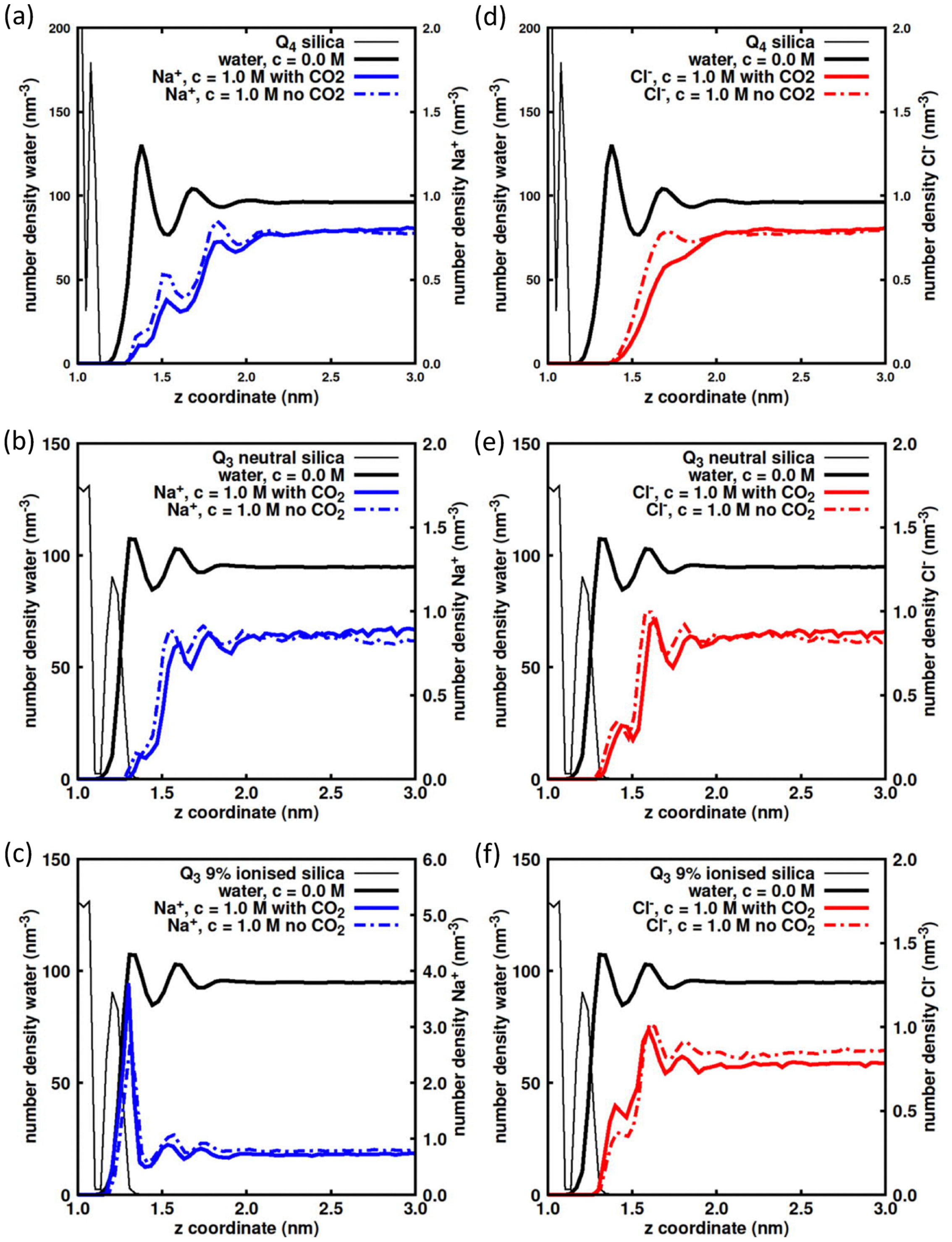

Fig. 12 Structure of the innermost part of the EDL. Shown are data obtained under CO_2-free conditions (dash-dotted lines) and in the presence of CO_2 (solid lines). The density profiles for Na^+ are shown in blue (left column), those of Cl^- are shown in red (right column). Data er for (a) and (d) uncharged Q4 silica, (b) and (e) uncharged Q3 silica, and (c) and (f) 9% ionized Q3 silica. Note the deviating scale for the Na^+ density in (c). As before, the black lines denote the profiles of water and of the surface atoms.

This is illustrated in Fig. 14 for the two silica Q3 surfaces. The situation without CO_2 is shown in the left column [(a) and (c)], while the right column shows the situation in the presence of CO_2 [(b) and (d)]. In the upper Fig. 14(a) and (b) we replot the ionic density profiles for Na^+ and Cl^- at the neutral Q3 surface, now overlaid by the total accumulated charge (green line). Overall charge-neutrality is retained, except for a very slight charge oscillation due to the slightly differing locations of the

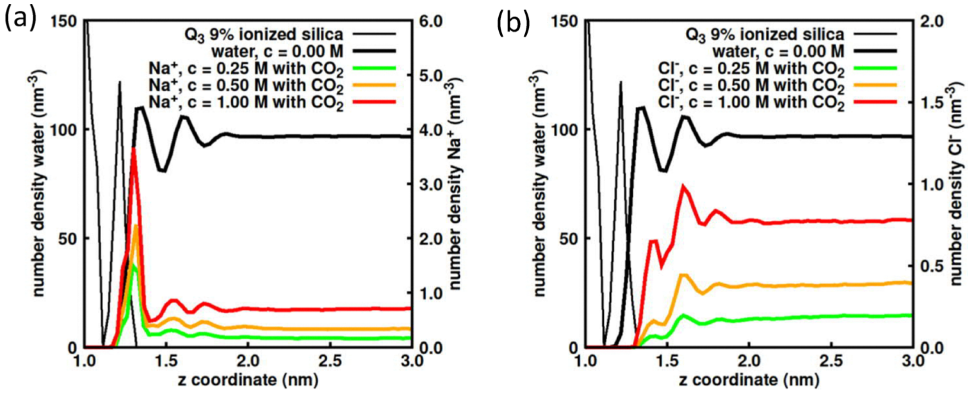

Fig. 13 Salt dependence of the ionic structure. Shown are data obtained for 9% ionized silica Q3 in the presence of CO_2. The density profiles for Na^+ are shown in (a), those of Cl^- in (b). Different line colors denote different salt concentrations as indicated in the key. As before, the black lines denote the profiles of water and of the surface atoms.

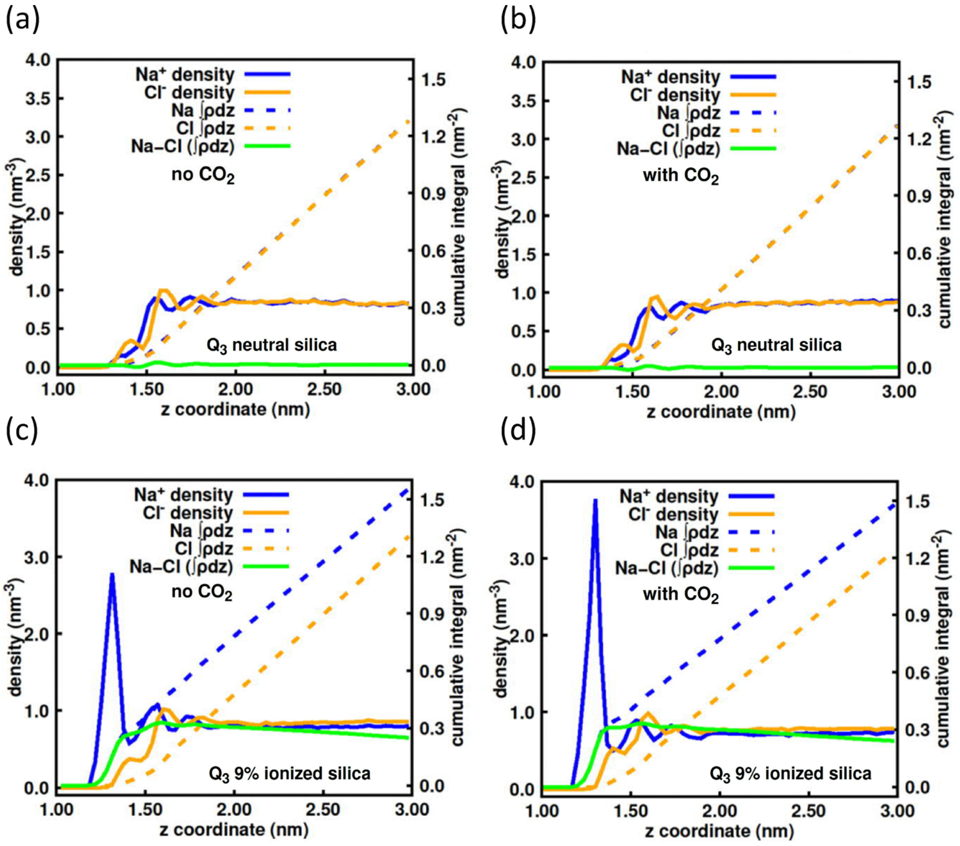

Fig. 14 Charge imbalance due to EDL structuring at silica Q3. Ion density profiles of Na^+ (blue solid lines) and Cl^- (dark yellow solid lines), corresponding integrated densities (dashed lines) and resulting charge imbalance (green line). The charge neutral surface is shown in (a) and (b) without and with CO_2, respectively. Except for a very mild charge oscillation, electro neutrality is retained. The 9% ionized surface is shown in (c) and (d) without and with CO_2, respectively. Roughly 70% of the surface charge is compensated by counter-ion accumulation in the first layer.

density maxima for cations and anions. The lower Fig. 14(c) and (d) show how across the 1st Na^+ density maximum, the integrated charge imbalance increases. In the absence of CO_2, the increase is steep at first, but continues in a weakened form out to the third Na^+ layer. In the presence of CO_2, the increase is sharper, rather steplike and is followed by a plateau-like region. The sharpening is due to the CO_2-induced increase of the ion density for the first Na^+ layer. Beyond the third Na^+ layer, the integrated charge imbalance decreases again, albeit very slowly. This is due to the slightly larger density in the outer regions which presumably is an effect of the finite simulation volume.

The maximum integrated charge imbalance in Fig. 14(c) and (d) amounts to about 0.3 nm^{-2} irrespective of the presence of CO_2. For comparison, at a 9% ionized Q3, we have a surface charge density of 0.423 nm^{-2}. This shows that about 70% of the surface charge is compensated by counter-ion "condensation" within the first 2 nm from the surface. For the CO_2-free case, we may further compare this number to the percentage of freely mobile counter-ions derived from conductivity, which was 23.5% and to the ratio of effective to bare charge observed in the PBC calculations, which was 21%. This good qualitative agreement is striking and supports our above interpretation of the conductometric experiments.

In none of our simulations, did the addition of salt lead to charging by co-ion adsorption. In particular the findings in Fig. 14(c) and (d) are in line with the experimentally observed absence of Cl^- type co-ion adsorption at fused silica. However, they also indicate, that the co-ion structuring gets more pronounced in the presence of CO_2. It will be interesting to explore in future simulation studies, what happens upon exchange of Br^- or I^- for Cl^- as co-ion. Overall, our new simulations confirm the pronounced accumulation of molecular CO_2 at various surfaces. They furthermore demonstrate the surface-specific structure of the innermost EDL and the interesting changes introduced therein by the presence of CO_2.

Discussion

The present investigations relied on three major advances. First, using ion exchange for decarbonization, we could unequivocally identify CO_2 as an active agent in the observed charge variations. This relied on the selective removal of CO_2 not possible in previous work employing degassing techniques.[15,20,22,23,27–32] Regardless of the presence of N_2 and O_2 (and other inert gases) in solution, a change in the state of surface charge is only observed for the selective removal of CO_2. Second, the here used closed, gas-tight tubing system with *in situ* control of electrolyte composition using parallel conductivity and photometric pH-determination not only assured reproducible sample conditioning. It also allowed for systematic experiments in dependence on CO_2 content covering the range from thoroughly decarbonized to over-carbonized, *i.e.* equilibrated against nearly pure CO_2 atmosphere. To the best of our knowledge this represents the first set of studies quantifying the influence of CO_2 on surface charges. Third, the electrokinetic experiments were carried out using multiple scattering free LDV in a cell featuring exchangeable side walls. This allowed simultaneous measurements of two (or even three) different surfaces under identical conditions. We thus could reliably compare hydrophilic silica surfaces to hydrophobic polymer surfaces. However, we could also exchange the silica specimen for sapphire while keeping the polymer tracers. The presented improvements allowed a flexible arrangement of our systematic experiments and facilitated comprehensive investigations on a reasonable time scale.

Our most important results obtained so far are the following. On the experimental side, we observed: (i) a drastic decharging at surfaces stabilized by weakly acidic groups in the presence of CO_2 which went far beyond the known effects of the CO_2 dissociation products. (ii) Under over-carbonized conditions, a near complete decharging of the polymeric surface and a corresponding loss of counter-ion condensation and counter-ion exchange. (iii) An assistance of the charging process at nominally charge-neutral oxide surfaces by the presence of CO_2. (iv) A pronounced promotion of co-ion adsorption in the presence of CO_2.

The main findings of our simulations were: (i) a clear tendency of molecular CO_2 to enrich at most different solid surfaces in a thin diffusive layer. (ii) A moderate surface specifity: CO_2 enrichment was most pronounced at charge neutral hydrophobic surfaces, somewhat less at the charge-neutral hydrophilic surface and even lower but still significant at hydrophilic charged surfaces. (iii) An assistance of enrichment at neutral surfaces by the presence of salt. (iv) An enrichment of CO_2 in the vicinity of the first water layer. Peak enrichment occurs below that water layer for the hydrophobic organic surface, practically coincident for the hydrophobic oxide surface and slightly above for the hydrophilic surface. In all cases, however, the enrichment is detectable in a weakened form out to the second water layer (v) An induction of significant changes of the EDL structure by CO_2: Both the depletion of ions at uncharged surfaces and the layered enrichment at charged surfaces are enhanced in the presence of CO_2. (vi) No co-ion adsorption for Cl^- as co-ion.

This comprehensive data set is now used to develop a consistent interpretation of the Janus nature displayed by CO_2. We start from the observation that CO_2 was enriched at all simulated surfaces (Fig. 10). We further note that the structural details of the innermost part of the EDL are determined by the interplay of steric, electrostatic and dipolar interactions, as well as quantum mechanics as far as the H-bond network is concerned. Compared to the bulk of the electrolyte, the bulk materials of all studied surfaces (SiO_2 or Isoleucine) feature a much lower dielectric permittivity. We therefore attribute the CO_2 enrichment to van der Waals attraction. Since CO_2 is electrically neutral, steric interactions are responsible for its final location. CO_2 is able to enrich below the first water layer in the hydrophobicity related gap at the organic charge neutral surface [Fig. 10(a)]. This conclusion is in line with previous reports from theory, experiment and simulation.[19–21] However, due to its small size,[51] CO_2 also can be easily incorporated in the interstitials of a hydrogen bond network. Therefore, the main peak is also seen close to the 1st layer of water, when the latter is closer to the surface for less hydrophobic surfaces [Fig. 7(b) and (c)]. Furthermore, the enriched molecules interact sterically with the ionic EDL components. The presence of CO_2 simply increases their depletion, be it Na^+ or Cl^- [Fig. 9(a), (b), (e) and (f)]. Taking the simulation results together with our experimental findings (i) to (iv), our first main conclusion is the observed massive changes in the charge of our surfaces are caused by the presence of molecular CO_2 in the innermost part of the EDL.

Dielectric charge regulation

For the following discussion we assume that the increased presence of molecular CO_2 leads to a locally decreased dielectric permittivity. This will strengthen all electrostatic interactions within the innermost part of the EDL. We first discuss the consequences for surfaces charged by weakly acidic groups. Here, strengthened electrostatics can influence the degree of dissociation in two closely related ways. This is illustrated schematically in Fig. 15. We suppose that the presence of CO_2 decreases the dielectric constant locally. A rough estimate from Fig. 8 gives an initial decrease by no more than 2%. However, this is enough to induce increased intra-molecular and inter-molecular electrostatic interactions within and between surface groups. The former will slightly increase the energy needed for dissociation, the latter increases the Bjerrum length, λ_B and introduces a Coulomb penalty exceeding k_BT for surface groups separated by less than that length. Together, this will lead to a mild reduction of the degree of dissociation. Comparing Fig. 10(c) and (d), however shows that the amount of enriched CO_2 is increased, as the charge is lowered. This enables a feedback loop leading to further decreased dissociation degrees. Its saturation value is set by the chemical nature of the surface groups and the maximum amount of CO_2 available for enrichment. The former is seen comparing the start points of titration in Fig. 7(a) and (b). Upon going from decarbonized over ambient to over-carbonized conditions, the initial charge is halved for the silica surface, while a near complete decharging of the carboxylated surface occurs under over-carbonized conditions. We stress again, that this drastic decharging cannot be explained by the well-known pH-driven charge regulation,[35] which determines the charge state of this surface in the absence of CO_2. Its effect due to the decreased pH upon allowing ambient CO_2 is clearly visible but insufficient to explain the observed amount of decharging. Therefore, the here sketched CO_2-induced mechanism is independent and acts in addition. We have provisionally termed the novel mechanism dielectric charge regulation.[82]

Charging of a H-bond network

We now turn to nominally uncharged surfaces. Sapphire (0001) bears Al_2OH groups, which, in principle can be protonated or deprotonated. This, however does not occur in the pH ranges probed in the present study. We may therefore consider sapphire (0001) to effectively carry no ionogenic groups. Further, there are no salt ions present, which could be adsorbed to the surface. Still, the surface shows a moderate charge when immersed in decarbonized and deionized water at pH-neutral conditions (Fig. 9). The spontaneous charging of nominally neutral surfaces is well documented with the details depending on pH, salinity and cleaning procedure.[11–13,29–32,118,119] Based on *ab initio* molecular dynamics simulations, recent work has argued, that charging of this surface proceeds *via* the enrichment of hydroxid ions captured from the bulk into the hydrogen bond network of the first layer.[14] We can support this picture from our simulation results, where the enrichment of CO_2 at charge-neutral surfaces became very pronounced (Fig. 10) and was further increased by the presence of background salt (Fig. 11). For the neutral Q4 surface, peak densities reached values of up to 30 times the bulk density at the location of the first water layer. This means that about one fifth of the total density at that location is contributed by CO_2. We recall that the Q4 surface was chosen for its similarity to sapphire (0001) as it is also hydrophobic, neutral, and not bearing any ionogenic surface groups. We therefore infer that also at sapphire (0001), there should be a significant enrichment of molecular CO_2 coinciding with the location of the innermost water layer.

This will lead to a substantial strengthening of the Coulomb contribution in the H-bond network and specifically between water and OH^-, which provides additional binding sites. Its integration into the network then leads to the experimentally observed increase in negative charge (Fig. 8). Alternatively, one

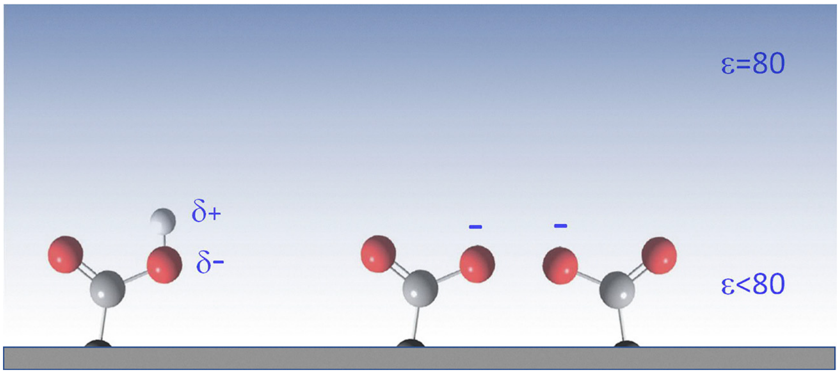

Fig. 15 Scheme of dielectric charge regulation. Intra-molecular (left) and inter-molecular (right) Coulomb interactions are considered for a surface charged by weakly acidic groups. At lowered dielectric permittivity of the embedding medium, O–H-bonds will be strengthened, which in turn will increase the dissociation energy. Repulsion between neighboring surface charges will be increased, leading to an extra Coulomb energy for closely spaced groups.

may think of CO_3H^- being incorporated, as under ambient conditions and pH 5.5 its concentration amounts to about one tenth of that of molecular CO_2, which is about two orders of magnitude larger than that of bulk OH^-.[120] We therefore suggest that future *ab initio* molecular dynamics simulations focus on the effect that CO_2 has on the incorporation of OH^- into or bicarbonate on top of the H-bond network. Regarding the charging of inert oxide surfaces, our study is clearly preliminary. Further ζ-potential determinations under variation of pH and salinity are highly desired just as corresponding simulations to support our hypothesis. For the time being, we believe that an enhancement of surface charging *via* an increased incorporation of H-bridge forming ions based on a locally increased dielectric permittivity yields a consistent explanation our experimental observations.

Adsorption of OH^- into the first water layer has also been proposed as responsible for the negative charge of oil droplets in water.[30] ζ-potentials of droplets in degassed water range between some 50 mV and some 90 mV in magnitude,[121] potentials in emulsions equilibrated against ambient air could not be measured due to their instability against coalescence. If our observation of an increased ζ-potential at a chemically inert, hydrophobic surfaces in the presence of CO_2 is transferrable to oil-in-water emulsions, one would expect a further stabilization, if CO_2 is admitted. This, however, is not observed. Rather, it is the removal of dissolved gas which stabilizes the emulsions.[30] The comparison of existing experimental data on oil droplets and the present results therefore supports the idea of an additional medium-ranged hydrophobic attraction causing coalescence. Since such a comparison is inconclusive regarding the gas species responsible for hydrophobic effects, it would be very interesting to repeat the experiments on oil-in-water emulsions using selective removal CO_2 by ion exchange. This should show, whether the effects are caused by CO_2 or any of the other atmospheric gases.

Co-ion adsorption

In the experiments, we saw a CO_2-supported switch from purely screening behavior of co-ions – reducing the effective surface charge – to a pronounced adsorption – leading to a significant recharging of surfaces formerly discharged by dielectric charge regulation. Specifically, in Fig. 7, we observed that for the hydrophobic surface, this switch was triggered by lower amounts of CO_2. In Fig. 8, we can discriminate ion-specific effects: in general, larger ions are more easily adsorbed. Again, this is surface specific. At the hydrophobic surface, only Cl^- and F^- adsorb under decarbonized conditions, while all four co-ions recharge it at ambient CO_2 conditions. The hydrophilic surface does not adsorb any ion under decarbonized conditions, but is recharged by Cl^- and F^- after equilibration in contact with air. This raises the question, what lies behind the ability of molecular CO_2 to induce ion- and surface-specific co-ion adsorption.

Co-ions are known to adsorb unspecifically at surfaces. Different reasons have been discussed which range from chaotropic behavior with respect to bulk water, over dispersion forces and hydrophobic effects to ion–ion correlations.[3–6,122–124] Since different interaction types are involved and may compete at different surfaces, no general consensus has as yet been established. We here, however, are interested in elucidating the role of CO_2 in supporting the adsorption of co-ions. To answer this question, we reconsider Fig. 12(c). There, we see, that CO_2 triggers a moderately increased enrichment of counter-ions. We propose that this is caused by increased electrostatic attraction to the charged surface. Moreover, in Fig. 12(f), we observe a pronounced increase of the co-ion density as compared to the CO_2-free case. Recalling that the region of significantly enhanced CO_2-density extends at least out to the second water layer [Fig. 10(d)], we conclude, that its presence – inducing a locally decreased dielectric permittivity – also enhances the electrostatic attraction of co-ions towards the counter-ion layer. In addition, the increased population within the sodium layer will screen the repulsion between surface and co-ions more strongly. In Fig. 12(f), the main Cl^- maximum is located at a distance where without CO_2 we still see steric effects, which at neutral Q4 [Fig. 12(b)] are even strong enough to prevent any Cl^- layering. Clearly, the enhancement of EDL structuring is dominated by electrostatic ion correlations overwhelming steric interactions. This is also seen in Fig. 10, illustrating the additional influence of increased salt concentrations. For both ions we can see a transition from a still underlying diffuse accumulation, respectively depletion to a clear structuring with several clearly discernible maxima and minima. In each case, the strongest relative increase occurs for the first ionic layer.

Fig. 11 shows that this increase in EDL structuring does not yet lead to a net adsorption of co-ions and thus to an increase of charge. Except for the surplus of counter-ions balancing the surface charges, the mobile part of the EDL remains electrically neutral, in line with the experimental observation in Fig. 5(a) and (c). We stress, however, that charging is observed experimentally, once we move to more hydrophobic surfaces and/or to larger co-ions. Clearly, additional simulations for larger co-ions remain to be performed to reproduce the screening-charging transition *in silico*. Already now, however, we can conclude that the simulations strongly support our suggestion of a decreased dielectric permittivity and as a consequence an increased electrostatically promoted EDL structuring by ion–ion correlations.

We anticipate, that our findings have effects also on the adsorption of larger co-ionic species, like multivalent co-ions, surfactants and other large co-ions as well as proteins.[59,125] In fact, they can be used to explain the failure of particle charging by surfactant under thoroughly deionized and decarbonized conditions.[60] We note that the CO_2 induced enhancement of ion correlations in the first place requires a charged interface for counter-ion enrichment as a remarkable general feature of charging by co-ion adsorption. At neutral surfaces by contrast, Fig. 12(a), (d), (b) and (e) show that either there is no strong correlation or, if some correlation is present, it remains similar in magnitude and is only shifted slightly in position. This in turn prevents charging by direct co-ion adsorption stemming from added salt. There, however, the enhanced electrostatics appear to strengthen the H-bond network and facilitate the charging by incorporation of OH^- stemming from water hydrolysis.

Conclusion

We here gave an overview on a series of precision experiments monitoring the charge state of representative surfaces in contact with aqueous electrolytes. We focused on the influence of dissolved CO_2 added by equilibrating initially de-carbonized systems in contact with atmospheres of controlled CO_2 concentration. Using ion-exchange for selective de-carbonization of systems equilibrated against atmospheres of different CO_2 content allowed to attribute observed effects to CO_2 and rule out other gases as cause. Working at de-ionized or low salt conditions, *i.e.*, in the absence of masking buffers, we demonstrated that the effects of molecular CO_2 may be significantly larger than the known effects of its dissociation products. Moreover, we could demonstrate the Janus nature of molecular CO_2 in charge regulation at surfaces immersed in aqueous electrolytes. Depending on the surface under investigation CO_2 assists charging, de-charging and/or recharging. This is in stark contrast to the influence of its dissociation products, which always cause decharging only. Thus, in a given situation, the effects of molecular and dissociated CO_2 may oppose, *e.g.*, upon increasing the amount of dissolved CO_2 in a deionized system.

Remarkably, the effects of molecular CO_2 had been neglected in previous work. In fact, we anticipate that our findings are of relevance in many fundamental studies, where the exclusion of CO_2 often remains an unmet challenge. If molecular CO_2 is able to affect interfacial charge, the question comes up to what extent many of the fundamental studies have been carried out under well-controlled conditions. However, with the instrumental developments reported, our approach paves the way for further such studies with reliably controlled CO_2 content.

We complemented the experiments by simulations on representative surfaces under similar conditions. The two main findings are the strong tendency of molecular CO_2 to adsorb at most different surfaces and the significant influence it has on the resulting EDL structure and the interactions amongst EDL constituents. We suggest a common cause for the Janus-type charge-manipulation phenomenology displayed by molecular CO_2, namely strongly enhanced electrostatics triggered by a local decrease in dielectric permittivity. Based on this assumption we can consistently interpret our experimental findings as being due to the presence of diffusely adsorbed molecular CO_2, and explain the specific outcomes in their dependence on the involved charging mechanism and constituents: chemically inert hydrophobic surfaces show an increased effective charge presumably resulting from a strengthened H-bond network incorporating OH^- ions. Surfaces bearing weakly acidic groups display a reduced degree of dissociation due to dielectric charge regulation. And for weakly charged surfaces, our simulations suggest that ion correlations can facilitate (re-)charging by co-ions adsorbing adjacent to the first counter-ion layer.

We anticipate that our overview should stir much additional experimental interest, and, at the same time, pave the way to realize it. Employing the described advanced conditioning procedures, future charge characterization experiments may therefore consider further surface types like *e.g.*, metals or proteins, as well as additional charging/decharging mechanisms. An important contribution would be an experimental confirmation and quantification of diffuse CO_2 adsorption at surfaces, be it by scattering or spectroscopic techniques. The present overview, in addition, provides some major challenges to theory and simulation, too. *E.g.*, dielectric charge regulation calls for a suitable theoretical treatment possibly following, but going beyond the qualitative arguments introduced here. Suitable force fields for larger co-ions should facilitate tests of CO_2 assisted co-ion adsorption within the EDL, *e.g.*, for Br^- and I^-, which are currently not included in CHARMM27. The suggestions made for the enhanced charging of inert surfaces could be tested in future *ab initio* molecular dynamics simulations in the presence of molecular CO_2.

Accepting the suggestion of CO_2-enhanced local interactions, we expect profound effects also for other issues with strong electrostatic contributions: surface reactions in general, catalysis in particular, but also CO_2 sequestering or membrane properties. Again, a Janus nature may be envisioned, depending on whether CO_2 acts preferably on binding and release of species or modifies their reactivity. Charge state and EDL structure also play a vital role for many physical properties of surfaces related to wetting or surface mobility. For systems with overlapping EDLs, *e.g.*, membrane pores, the presence or absence of CO_2 possibly provides a convenient switch between states.

Overall, our complementary experimental and theoretical investigations demonstrate that molecular CO_2 isn't the harmless neutral molecule it was taken to be. We anticipate that future investigations following this line will lead to a much-refined understanding of the here-shown Janus nature of CO_2, and, in the long run, will find many interesting applications.

Author contributions

Conceptualization: TP, PV, MNQ, CH. Experiments: PV, MR, JL. Numerical simulations: MNQ. Theory: DB, CH. Data analysis: PV, MNQ, MR. Supervision: TP, MS, CH. Writing original draft: PV, TP. Writing review and editing: TP, PV, MNQ, JL, DB, MS, CH.

Conflicts of interest

There are no conflicts of interest to declare.

Data availability

Original data are available from the authors upon reasonable request.

Supplementary information (SI) is available. See DOI: https://doi.org/10.1039/d6sm00222f.

Acknowledgements

We dedicate this overview to our late colleague Stefan U. Egelhaaf to express our special gratefulness to him. He was an excellent experimenter and exceptional teacher with unrivalled expertise in optical heterodyning and much experience in controlling the boundary conditions in colloidal suspensions. Accompanied by many fruitful discussions with Stefan we could substantially improve our instrumental approach and apply it to well conditioned samples. Sadly, he passed away early 2024 and cannot anymore witness the present advances in exploring CO_2-related issues. We are also indebted to M. Medebach, D. Botin, J. Wenzel, R. Niu, N. Möller, L. Marota Mapa, H. Schweinfurth, C. Wittenberg. S. Juretzka and S. Okomura for their contributions to the experimental developments. We further thank H. J. Butt, A. Delgado, F. Carrique, B. Liebchen, J. Yamanaka, and Y. Levin for their continued interest and numerous fruitful discussions of charge related issues. Financial support of the Deutsche Forschungsgemeinschaft (DFG) Grant no. Pa459/23-1 is gratefully acknowledged.

References

1 J. Lyklema, *Fundamentals of Interface and Colloid Science: Solid–Liquid Interfaces*, Academic Press, London, 1995.
2 J. Lyklema, *Colloids Surf., A*, 2001, **291**, 3–12.
3 C. M. Ma, F. J. Micale, M. S. El-Aasser and J. W. Vanderhoff, *ACS Symp. Ser.*, 1981, **165**, 251–262.
4 B. R. Midmore and R. J. Hunter, *J. Colloids Interface Sci.*, 1988, **122**, 521–529.
5 M. Hartenstein, A. Weiss, S. Seelenmeyer and M. Ballauff, *J. Colloid Interface Sci.*, 1998, **208**, 266–271.
6 B. Uzelac, V. Valmacco and G. Trefalt, *Soft Matter*, 2017, **13**, 5741–5748.
7 M. L. Jiménez, Á. V. Delgado and J. Lyklema, *Langmuir*, 2012, **28**, 6786–6793.
8 T. Palberg, W. Mönch, F. Bitzer, T. Bellini and R. Piazza, *Phys. Rev. Lett.*, 1995, **74**, 4555–4558.
9 R. Dong, Q. Zhang, W. Gao, A. Pei and B. Ren, *ACS Nano*, 2015, **10**, 839–844.
10 X. Li, P. Bista, A. Z. Stetten, H. Bonart, M. T. Schür, S. Hardt, F. Bodzioni, H. Marschall, A. Saal, X. Deng, R. Berger, S. A. L. Weber and H.-J. Butt, *Nat. Phys.*, 2022, **18**, 713–719.
11 N. Agmon, H. J. Bakker, R. K. Campen, R. H. Henchman, P. Pohl, S. Roke, M. Thämer and A. Hassanali, *Chem. Rev.*, 2016, **116**, 7642–7672.
12 H. Fang, W. Wu, Y. Sang, S. Chen, X. Zhu, L. Zhang, Y. Niu and W. Gan, *RSC Adv.*, 2015, **5**, 23578–23585.
13 K. G. Marinova, R. G. Alargova, N. D. Denkov, O. D. Velev, D. N. Petsev, I. B. Ivanov and R. P. Borwankar, *Langmuir*, 1996, **12**, 2045–2051.
14 Y. Zhang, Y.-B. Zhuang, X. Liu, J. Cheng, J. Lützenkirchen and X. Lua, *Chem. Commun.*, 2024, **60**, 9113–9116.
15 G. V. Franks, *J. Colloid Interface Sci.*, 2002, **249**, 44–51.
16 J. Yamanaka, Y. Hayashi, N. Ise and T. Yamaguchi, *Phys. Rev. E*, 1997, **55**, 3028–3036.
17 P. Wette, I. Klassen, D. Holland-Moritz, D. M. Herlach, H. J. Schöpe, N. Lorenz, H. Reiber, T. Palberg and S. V. Roth, *J. Chem. Phys.*, 2010, **132**, 131102.
18 M. Shinohara, A. Toyotama, M. Suzuki, Y. Sugao, T. Okuzono, F. Uchida and J. Yamanaka, *Langmuir*, 2013, **29**, 9668–9676.
19 P. Scharlin, R. Battino, E. Silla, I. Tuñón and J. L. Pascual-Ahuirc, *Pure Appl. Chem.*, 1998, **70**, 1895–1904.
20 D. A. Doshi, E. B. Watkins, J. N. Israelachvili and J. Majewski, *Proc. Natl. Acad. Sci. U. S. A.*, 2005, **102**, 9458–9462.
21 S. M. Dammer and D. Lohse, *Phys. Rev. Lett.*, 2006, **96**, 206101.
22 X. H. Zhang, A. Khan and W. A. Ducker, *Phys. Rev. Lett.*, 2007, **98**, 136101.
23 H. Peng, G. R. Birkett and A. V. Nguyen, *Langmuir*, 2013, **29**, 15266–15274.
24 E. Johnson and S. Haussener, *J. Phys. Chem. C*, 2024, **128**, 10450–10464.
25 R. Ding, A.-R. Siddiqui, K. Martin, J. N'Diaye, J. B. Varley, J. Dawlaty, J. Rodríguez-López and V. Augustyn, *ACS Electrochem.*, 2025, **1**, 476–485.
26 L. Huang, C. Ling, L. Zhou, W. Liang, Y. Huang, L. Zhang, P. Maitarad, D. Zang and C. Wang, *Chin. Phys. B*, 2025, **34**, 014701.
27 I. Siretanu, J. P. Chapel and C. Drummond, *ACS Nano*, 2011, **5**, 2939–2947.
28 B. İlhan, C. Annink, D. V. Nguyen, F. Mugele, I. Siretanu and M. H. G. Duits, *Colloids Surf., A*, 2019, **560**, 50–58.
29 M. Alfridsson, B. Ninham and S. Wall, *Langmuir*, 2000, **16**, 10087–10091.
30 N. Maeda, K. J. Rosenberg, J. N. Israelachvili and R. M. Pashley, *Langmuir*, 2004, **20**, 3129–3137.
31 J. Eastoe and C. Ellis, *Adv. Colloid Interface Sci.*, 2007, **134–135**, 89–95.
32 B. W. Ninham, R. M. Pashley and P. Lo Nostro, *Curr. Opn. Colloid Interface Sci.*, 2017, **27**, 25–32.
33 F. J. Millero, R. Feistel, D. G. Wright and T. J. McDougall, *Deep Sea Res., Part I*, 2008, **55**, 50–72.
34 F. Carrique, E. Ruiz-Reina, R. Roa, F. J. Arroyo and Á. V. Delgado, *J. Colloid Interface Sci.*, 2015, **455**, 46–54.
35 S. H. Behrens and M. Borkovec, *J. Chem. Phys.*, 1999, **111**, 382–385.
36 M. Heinen, E. Allahyarov and H. Löwen, *J. Comput. Chem.*, 2014, **35**, 275–289.
37 M. Heinen, T. Palberg and H. Löwen, *J. Chem. Phys*, 2014, **140**, 124904.

38 D. Al Mahrouqi, J. Vinogradov and M. D. Jackson, *Adv. Colloid Surf. Sci.*, 2017, **240**, 60–76.
39 G. Trefalt, S. H. Behrens and M. Borkovec, *Langmuir*, 2016, **32**, 380–400.
40 G. Trefalt, T. Palberg and M. Borkovec, *Curr. Opin. Colloid Interface Sci.*, 2017, **27**, 9–17.
41 S. Jailani, G. V. Franks and T. Healy, *J. Am. Ceram. Soc.*, 2008, **91**, 1141–1147.
42 A. Delgado, F. González-Caballero, R. J. Hunter, L. K. Koopal and J. Lyklema, *J. Colloid Interface Sci.*, 2007, **309**, 194–224.
43 D. Hessinger, M. Evers and T. Palberg, *Phys. Rev. E*, 2000, **61**, 5493–5506.
44 L. Bocquet, E. Trizac and M. Aubouy, *J. Chem. Phys*, 2002, **117**, 8138–8152.
45 Y. Levin and Rep Prog, *Phys.*, 2002, **65**, 1577–1632.
46 R. Klein, H. H. v Grünberg, C. Bechinger, M. Brunner and V. Lobashkin, *J. Phys.: Condens. Matter*, 2002, **14**, 7631–7648.
47 L. Shapran, M. Medebach, P. Wette, H. J. Schöpe, T. Palberg, J. Horbach, T. Kreer and A. Chaterji, *Colloids Surf. A*, 2005, **270**, 220–225.
48 L. Shapran, H. J. Schöpe and T. Palberg, *J. Chem. Phys*, 2006, **125**, 194714.
49 D. C. Carrascal-Hernandez, M. Mendez-Lopez, D. Insuasty, S. García-Freites, M. Sanjuan and E. Márquez, *Gels*, 2024, **10**, 386.
50 M. Shen, W. Guo, L. Tong, L. Wang, P. K. Chu, S. Kawi and Y. Ding, *Chem. Soc. Rev.*, 2025, **54**, 2762–2831.
51 R. L. Beil and R. J. Hinde, *Theor. Chem. Acc.*, 2021, **140**, 120.
52 K. Ariga, H. Ito, J. P. Hill and H. Tsukube, *Chem. Soc. Rev.*, 2012, **41**, 5800–5835.
53 Á. V. Delgado, F. Carrique, R. Roa and E. Ruiz-Reina, *Curr. Opn. Colloid Interface Sci.*, 2016, **24**, 32–43.
54 R. W. O'Brien and L. R. White, *J. Chem. Soc., Faraday Trans. 2*, 1978, **74**, 1607–1629.
55 N. Garbow, M. Evers, T. Palberg and T. Okubo, *J. Phys.: Condens. Matter*, 2004, **16**, 3835–3842.
56 V. Lobashkin, B. Dünweg, C. Holm, M. Medebach and T. Palberg, *Phys. Rev. Lett.*, 2007, **98**, 176105.
57 H. Reiber, T. Köller, T. Palberg, F. Carrique, E. Ruiz-Reina and R. Piazza, *J. Colloid Interface Sci.*, 2007, **309**, 315–322.
58 D. Botin, F. Carrique, E. Ruiz-Reina and T. Palberg, *J. Chem. Phys.*, 2020, **152**, 244902.
59 A. Murakado, A. Toyotama, M. Yamamoto, R. Nagano, T. Okuzono and J. Yamanaka, *J. Colloid Interface Sci.*, 2015, **465**, 200–206.
60 S. Juretzka, Optische Experimente zu Verfestigungs- und Schmelzprozessen auf kolloidaler Skala, PhD thesis, Mainz, 2019.
61 C. N. Bensley and R. J. Hunter, *J. Colloids lnterface Sci.*, 1983, **92**, 448–462.
62 B. R. Midmore and R. J. Hunter, *J. Colloids Interface Sci.*, 1988, **122**, 521–529.
63 M. Elimelech and C. R. O'Melia, *Colloids Surf.*, 1990, **44**, 165.
64 A. Delgado, F. González-Caballero, M. A. Cabrerizo and I. Alados, *Acta Polym.*, 1987, **38**, 66–70.
65 I. Semenov, S. Raafatnia, M. Sega, V. Lobaskin, C. Holm and F. Kremer, *Phys. Rev. E*, 2013, **87**, 022302.
66 J. E. Seebergh and J. C. Berg, *Colloids Surf. A*, 1995, **100**, 139–153.
67 A. Martin-Molina, J. A. Maroto-Centeno, R. Hidalgo-Alvarez and M. Quesada-Perez, *Colloids Surf. A*, 2008, **319**, 103.
68 F. J. M. Ruiz-Cabello, M. Moazzami-Gudarzi, M. Elzbieciak-Wodka, P. Maroni, C. Labbez, M. Borkovec and G. Trefalt, *Soft Matter*, 2015, **11**, 1562–1571.
69 C. F. Zukoski and D. A. Saville, *J. Colloid Interface Sci.*, 1986, **114**, 32–44.
70 C. F. Zukoski and D. A. Saville, *J. Colloid Interface Sci.*, 1986, **114**, 45–53.
71 L. P. Voegtli and C. F. Zukoski, *J. Colloid Interface Sci.*, 1991, **141**, 92–108.
72 N. Garbow, M. Evers and T. Palberg, *Colloids Surf. A*, 2001, **195**, 227–241.
73 M. Deggelmann, T. Palberg, M. Hagenbüchle, E. E. Maier, R. Krause, C. Graf and R. Weber, *J. Colloid Interface Sci.*, 1991, **143**, 318–326.
74 T. Palberg, M. Medebach, N. Garbow, M. Evers, A. Barreira Fontecha, H. Reiber and E. Bartsch, *J. Phys. Condens. Matter*, 2004, **16**, S4039–S4050.
75 T. Palberg, W. Härtl, U. Wittig, H. Versmold, M. Würth and E. Simnacher, *J. Phys. Chem.*, 1992, **96**, 8180–8183.
76 P. Wette, H.-J. Schöpe, R. Biehl and T. Palberg, *J. Chem. Phys*, 2001, **114**, 7556–7562.
77 R. Niu, S. Khodorov, J. Weber, A. Reinmüller and T. Palberg, *NJP*, 2017, **19**, 115014.
78 *Aqion version 8.5.14 freeware program*, https://www.aqion.de/last access May 5, 2026.
79 T. Palberg, T. Köller, B. Sieber, H. Schweinfurth, H. Reiber and G. Nägele, *J. Phys.: Condens. Matter*, 2012, **24**, 464109.
80 D. Botin, L. Marota-Mapa, H. Schweinfurth, B. Sieber, C. Wittenberg and T. Palberg, *J. Chem. Phys*, 2017, **146**, 204904.
81 D. Botin, J. Wenzel, R. Niu and T. Palberg, *Soft Matter*, 2018, **14**, 8191–8204.
82 P. Vogel, N. Möller, M. N. Qaisrani, B. Pravash, S. Weber, H.-J. Butt, B. Liebchen, M. Sulpizi and T. Palberg, *J. Am. Chem. Soc.*, 2022, **144**, 21080–21087.
83 P. Vogel and T. Palberg, *J. Colloid Interface Sci.*, 2023, **656**, 280–288.
84 P. Vogel, D. Beyer, C. Holm and T. Palberg, *Soft Matter*, 2024, **20**, 9261–9272.
85 G. A. Parks, *Chem. Rev.*, 1965, **65**, 177–198.
86 M. Kosmulski, *Chemical Properties of Material Surfaces*, Marcel Dekker, New York, 2001.
87 T. Rabung, D. Schild, H. Geckeis, R. Klenze and T. Fanghänel, *J. Phys. Chem. B*, 2004, **108**, 17160–17165.
88 M. Medebach, R. Chuliá Jordán, H. Reiber, H.-J. Schöpe, R. Biehl, M. Evers, D. Hessinger, J. Olah, T. Palberg, E. Schönberger and P. Wette, *J. Chem. Phys*, 2005, **123**, 104903.

89 CRC handbook of chemistry and physics, ed D. R. Lide, *A ready-reference book of chemical and physical data*, CRC Press, Boca Raton, 76th edn, 1996.

90 R. Niu, P. Kreissl, A. T. Brown, G. Rempfer, D. Botin, C. Holm, T. Palberg and J. de Graaf, *Soft Matter*, 2017, **13**, 1505–1518.

91 N. Möller, B. Liebchen and T. Palberg, *Eur. Phys. J. E*, 2021, **44**, 41.

92 B. R. Ware, *Adv. Colloid Interface Sci.*, 1974, **4**, 1–44.

93 E. E. Uzgiris, *Prog. Surf. Sci.*, 1981, **10**, 53–164.

94 J. K. G. Dhont, *An introduction to the dynamics of colloids*, Elsevier, Amsterdam, 1996.

95 I. M. Tucker, J. C. W. Corbett, J. Fatkinb, R. O. Jack, M. Kaszuba, B. MacCreath and F. McNeil-Watson, *Curr. Opin. Colloid Interface Sci.*, 2015, **20**, 215–226.

96 T. Palberg and H. Versmold, *J. Phys. Chem.*, 1989, **93**, 5296–5301.

97 J. F. Miller, K. Schätzel and B. Vincent, *J. Colloid Interface Sci.*, 1991, **143**, 532–554.

98 M. Evers, N. Garbow, D. Hessinger and T. Palberg, *Phys. Rev. E*, 1998, **57**, 6774–6784.

99 H. Tanaka and T. Sonehara, *Rev. Sci. Instr*, 2002, **73**, 1998–2010.

100 G. Nägele, *Phys. Reports*, 1996, **272**, 215–372.

101 M. Medebach and T. Palberg, *Colloids Surf. A*, 2003, **222**, 175–183.

102 M. Deserno and C. Holm, in *Electrostatic Effects in Soft Matter and Biophysics. Proceedings of the NATO Advanced Research Workshop on Electrostatic Effects in Soft Matter and Biophysics Les Houches, France 1–13 October 2000*, ed. C. Holm, P. Kékicheff and R. Podgornik, Springer Netherlands, Imprint: Springer, Dordrecht, 1st edn, 2001, 27–52.

103 B. W. Ninham and V. A. Parsegian, *J. Theo. Biol.*, 1971, **31**, 405–428.

104 R. Podgornik, *J. Chem. Phys.*, 2018, **149**, 104701.

105 T. Colla, A. Bakhshandeh and Y. Levin, *J. Chem. Phys*, 2024, **161**, 094103.

106 P. Virtanen, R. Gommers, T. E. Oliphant, M. Haberland, T. Reddy, D. Cournapeau, E. Burovski, P. Peterson, W. Weckesser, J. Bright, S. J. van der Walt, M. Brett, J. Wilson, K. J. Millman, N. Mayorov, A. R. J. Nelson, E. Jones, R. Kern, E. Larson, C. J. Carey, İ. Polat, Y. Feng, E. W. Moore, J. VanderPlas, D. Laxalde, J. Perktold, R. Cimrman, I. Henriksen, E. A. Quintero, C. R. Harris, A. M. Archibald, A. H. Ribeiro, F. Pedregosa and P. van Mulbregt, *Nat. methods*, 2020, **17**, 261–272.

107 E. Trizac, L. Bocquet, M. Aubouy and H. H. von Grünberg, *Langmuir*, 2003, **19**, 4027–4033.

108 F. S. Emami, V. Puddu, R. J. Berry, V. Varshney, S. V. Patwardhan, C. C. Perry and H. Heinz, *Chem. Mater.*, 2014, **26**, 2647–2658.

109 C. H. Görbitz and B. Dalhus, *Acta Crystallogr., Sect. C: Cryst. Struct. Commun.*, 1996, **52**, 1464–1466.

110 W. L. Jorgensen, J. Chandrasekhar, J. D. Madura, R. W. Impey and M. L. Klein, *J. Chem. Phys*, 1983, **79**, 926–935.

111 A. D. MacKerell Jr, D. Bashford, M. Bellott, R. L. Dunbrack Jr, J. D. Evanseck, M. J. Field, S. Fischer, J. Gao, H. Guo and S. Ha, *et al.*, *J. Phys. Chem. B*, 1998, **102**, 3586–3616.

112 A. D. Mackerell Jr, M. Feig and C. L. Brooks III, *J. Comput. Chem.*, 2004, **25**, 1400–1415.

113 J. G. Harris and K. H. Yung, *J. Phys. Chem.*, 1995, **99**, 12021–12024.

114 G. Bussi, D. Donadio and M. Parrinello, *J. Chem. Phys*, 2007, **126**, 014101.

115 T. Darden, D. York and L. Pedersen, *J. Chem. Phys*, 1993, **98**, 10089–10092.

116 M. Parrinello and A. Rahman, *J. Appl. Phys*, 1981, **52**, 7182–7190.

117 S. Alexander, P. M. Chaikin, P. Grant, G. J. Morales, P. Pincus and D. Hone, *J. Chem. Phys*, 1984, **80**, 5776–5781.

118 J. Lützenkirchen, R. Zimmermann, T. Preočanin, A. Filby, T. Kupcik, D. Küttner, A. Abdelmonem, D. Schild, T. Rabung, M. Plaschke, F. Brandenstein, C. Werner and H. Geckeis, *Adv. Colloid Interface Sci.*, 2010, **157**, 61–74.

119 J. Lützenkirchen, G. V. Franks, M. Plaschke, R. Zimmermann, F. Heberling, A. Abdelmonem, G. K. Darbha, D. Schild, A. Filby, P. Eng, J. G. Catalano, J. Rosenqvist, T. Preocanin, T. Aytug, D. Zhang, Y. Gan and B. Braunschweig, *Adv. Colloid Interface Sci.*, 2018, **251**, 1–25.

120 X. Yan, M. Delgado, J. Aubry, O. Gribelin, A. Stocco, F. Boisson-Da Cruz, J. Bernard and F. Ganachaud, *J. Phys. Chem. Lett.*, 2018, **9**, 96–103.

121 T. K. Boyson and R. M. Pashley, *J. Colloid Interface Sci.*, 2007, **316**, 59–65.

122 A. Y. Grosberg, T. T. Nguyen and B. I. Shklovs, *Rev. Mod. Phys.*, 2002, **74**, 329–345.

123 Y. Zhang and P. S. Cremer, *Curr. Opin. Chem. Biol.*, 2006, **10**, 658–666.

124 W. Kunz, P. Lo Nostro and B. W. Ninham, *Curr. Opn. Colloid Interface Sci.*, 2004, **9**, 1–18.

125 B. Uzelac, V. Valmacco and G. Trefalt, *Soft Matter*, 2017, **13**, 5741–5748.